Preprint Title	A Comparative Study on the Photocatalytic Efficiency of ZnO, TiO_2 Nanoparticles and ZnO-TiO_2 Nanocomposites in Degrading Pharmaceutical Pollutants.
Authors	Manali Kaladagi, Vaishnavi Umbrajkar, sagar khater, Krushna Zoting, Haribhau Gholap and Maya Khater
Publication Date	19 Jan 2026
Article Type	Full Research Paper
ORCID® iDs	Vaishnavi Umbrajkar - https://orcid.org/0009-0002-2806-8202; Maya Khater - https://orcid.org/0009-0001-2882-4437

A Comparative Study on the Photocatalytic Efficiency of ZnO, TiO_2 Nanoparticles and ZnO-TiO_2 Nanocomposites in Degrading Pharmaceutical Pollutants.

Manali Kaladagi[*1],Vaishnavi Umbrajkar[‡1], Sagar Khater[‡2], Krushna Zoting[‡3], Haribhau Gholap[*3], Maya Khater[* 1]

[1]Department of Biotechnology, MES Abasaheb Garware College (Autonomous), Savitribai Phule Pune University, Pune 411004, India.

[2]Department of Microbiology, H. V. Desai College, Pune 411002, Savitribai Phule Pune University, Pune 411004, India.

[3]Department of Physics, Fergusson College (Autonomous), Savitribai Phule Pune University, Pune- 411004, India.

*Corresponding author: Dr. Maya Khater, e-mail:msk.agc@mespune.in

Dr. Haribhau Gholap, e-mail: haribhau.gholap@fergusson.edu

Abstract

Pharmaceutical drugs are now well established as persistent pollutants in aquatic ecosystems with ecological and human health hazards even at trace levels. Current treatments like biodegradation, adsorption and membrane filtration exhibit poor performance and high expense. Here, this approach provides a sustainable and efficient alternative by employing nanoparticle-based photocatalysts for degrading pharmaceuticals. Photocatalytic activities of ZnO and TiO_2 nanoparticles (NPs) purchased commercially, and the ZnO-TiO_2 nanocomposite prepared using the chemical precipitation method, were tested for their effectiveness against some chosen pharmaceutical contaminants like oxazolidinone antibiotics (Linezolid), Non-steroidal anti-inflammatory drug (NSAID) (Aspirin), and Paracetamol (Crocin). The prepared composite was studied to determine its structural and morphological characteristics. Experiments were performed under different pH, temperature, reaction time and agitation conditions for achieving optimal degradation efficiency. Reactive oxygen species (ROS) produced during the photocatalytic reaction were confirmed as major agents responsible for the oxidative degradation of the compounds. The process was found to perform best at pH 5, 30°C and 60°C (for Visible light and UV respectively) and 120 RPM and reached up to 75 - 80% degradation in 90 minutes. UV light markedly enhanced photocatalytic performance, particularly for Aspirin and Linezolid, with maximum degradation reaching 84.09% for Aspirin (ZnO) and 81.99% for Linezolid (TiO_2) under optimized conditions. Successful degradation was further validated by FTIR analysis of treated and untreated sample. All three nanomaterials

exhibited good photocatalytic activity, with varying effectiveness depending on the compound and experimental conditions. ZnO was superior in some instances: TiO_2 or the ZnO-TiO_2 composite was superior in others. The results indicate compound-specific optimization. Nanoparticle based photocatalysis offers a green, adaptable approach to degrade pharmaceuticals.

Keywords:

Pharmaceutical Drugs, Photocatalysis, Wastewater Treatment, ZnO-TiO_2 Nanoparticles

1.Introduction

Water is a basic requirement of all living things and contributes significantly to promoting ecological balance, climate regulation, and public health. Nevertheless, the alarm over water quality has increased with the advent of pharmaceutical contaminants (PCs), an important group of emerging contaminants (ECs) primarily derived from pharmaceutical industries. These biologically active substances, formulated to fight off, cure, or heal diseases, find their way into the environment unwittingly and have the potential to harm ecosystems and human health [1]. Drugs have emerged as a central pillar of contemporary medicine, and their use has increased exponentially over the past decades (35% increase between 2000 and 2010) as a result of the increasing global population, heavy investments in the healthcare industry, ongoing advances in biomedical research and extensive availability [2]. Detection of pharmaceutical compounds in aquatic and terrestrial environments has greatly enhanced with the advent of laboratory instrumentation and analytical techniques, such that sensitivity is now possible at levels ranging as low as micrograms per litre and, in others, even picograms per litre [3,4]. Even low concentrations, usually in the range of 1-500 ng/L, some drugs, particularly endocrine active compounds have been shown to disrupt aquatic ecosystems, leading to adverse effects on the physiology, reproduction and population dynamics of exposed species [5].These chemicals and their metabolic intermediates gain entry into aquatic environments via pathways such as municipal wastewater effluents, industrial effluents, aquaculture and livestock runoff and incomplete elimination in sewage treatment plants (STPs) [6] .Among these routes, urban wastewater is identified as the predominant worldwide source of pharmaceutical discharge and industrial production, hospitals, agriculture and aquaculture are significant contributors in given local contexts [7].

Worldwide research efforts have made an increasing emphasis on tracking pharmaceuticals in aquatic ecosystems. Of the chemicals most examined are estrogens, painkillers and antibiotics. UN region-wide surveys have indicated residues of at least 16 pharmaceuticals in surface water, groundwater, and even drinking water. Tetracyclines, especially, have routinely been found in the effluents of wastewater treatment plants globally. Diclofenac, which is used both in human medicine and veterinary medicine, appears to be the most common drug contaminant with confirmed presence in surface, ground and drinking water from 50 countries. Other compounds regularly found are the antiepileptic carbamazepine, the antibiotic sulfamethoxazole, and analgesics ibuprofen and naproxen [7].Surveillance of the Yamuna River passing through Delhi indicates that nine typical pharmaceuticals are year-round detectable, their concentrations varying by location and season, with sewage inputs and inadequate treatment being primarily responsible. Although environmental risks are low in short term, persistence and additive action of all environmental pharmaceuticals cause genuine concerns regarding long-term effects in aquatic organisms [8]. Likewise, recent studies on Bengaluru's Arkavathi River found ten Pharmaceutical and personal care products(PPCP) with ibuprofen, triclosan and diclofenac at highest concentrations and demonstrated evident seasonal variation associated with wastewater influents, with triclosan and diclofenac having ecological risks present even though no-short term human health issues were reported [9].

Apart from persistence, pharmaceutical pollutants pose serious threats to ecosystems and human health. PPCP effluents in aquatic systems have been associated with genetic damage, mutations, and harmful effects in a variety of species, including humans. Exposure can cause behaviour and reproduction disruption in aquatic organisms over long period of times. Particularly, Jukosky et.al. showed that male Japanese medaka (*Oryziaslatipes*) produced vitellogenin, a female-specific protein, following exposure to estrogenic substances [10]. Greater estrogenicity of water bodies has also been associated with increased fish mortality.5Furthermore, chronic exposure to PCs has been implicated in causing genetic mutations and behavioural changes among certain species [11,12]. The risks reach beyond animals to human, with waterborne drugs having the potential to pose health hazards to infants, the elderly, and patients suffering from kidney failure or liver failure. Another serious impact is the emergence of antimicrobial resistance (AMR) through continued release of antibiotics into the environment [13].

Efforts to mitigate pharmaceutical pollution have led to increased research on wastewater treatment technologies. Adsorption [14, 15], biological treatment [16], membrane-based

processes [17] and advanced oxidation processes have been investigated for decontaminating pharmaceutical wastewater. Other researchers have focused on the removal of pharmaceutical pollutants (PPs) in sewage treatment plants [18] and municipal wastewater, while others have investigated single treatment processes such as membrane bioreactors [16], constructed wetlands [19], adsorption methods [14] and biological-membrane-ultrasound systems [20]. While traditional processes like coagulation, flocculation, and reverse osmosis are widely used in wastewater treatment, their efficiency is hampered in intrinsic limitations. In the same way, the traditional aerobic biological processes are ineffective in biodegrading antibiotic polluted wastewater due to antimicrobial toxicity that inhibits microbial activity [21]. There have been studies indicating that traditional wastewater treatment technologies lack the ability to successfully remove pharmaceutical residues primarily because of their water solubility, low volatility, and biodegradation resistance [22].

As the limitations of conventional treatment techniques become ever more evident, researchers have turned to advanced oxidation processes (AOPs) as an extremely effective solution for organic pollutant degradation of wastewater, including pharmaceutical drugs [23]. The utility of AOPs is a result of their capacity to produce insitu hydroxyl radicals ($^{\bullet}OH$). Such radicals are one of the strongest oxidizing agents available, with a standard redox potential of ~2.80 V (only surpassed by fluorine), which makes them capable of non-selective attack and degradation of wide range of organic pollutants [24]. Among the various AOP approaches, photocatalysis has been especially of interest because it is effective and eco-friendly for the degradation of antibiotic contaminants. Its cost-effectiveness, combined with its ability to utilize natural sunlight and ambient conditions, renders it an attractive treatment approach to wastewater [25].The majority of antibiotics are resistant to degradation due to their stable molecular structures and therefore need the development of highly efficient photocatalysts with enhanced photocatalytic activity [26]. The most prevalent mechanisms of photocatalysis might be summarized in three simple steps: photon absorption, excitation and reaction. On absorption of photons by the photocatalyst with energy higher than its bandgap, electrons from the valence band (VB) are excited and transferred to the conduction band (CB), leaving a hole (h^+) in the valence band. Following the excitation, the holes and photoexcited electrons are successfully separated and move to the surface of the photocatalyst, where they initiate secondary reactions with adsorbed substances. In addition to this, photogenerated holes can directly interact with antibiotic molecules, driving their degradation and catalyzing the degradation of the harmful

pollutants [27,28] . Heterogeneous photocatalysis mostly depends on semiconducting materials like TiO_2, ZnO, and g-C_3N_4-based materials [29].

TiO_2 is the most applied photocatalyst because of its superior physical and chemical stability, high effectiveness, non-toxicity, and affordability [30]. Nanostructured TiO_2 also increases surface area and enhances degradation efficiency [31]. Anatase TiO_2, has a bandgap of around 3.2 eV, with the conduction band (CB) roughly around -0.51 V and valence band (VB) at about +2.69V, referenced to the normal hydrogen electrode (NHE) at neutral pH. Such energy alignment allows for the production of reactive oxygen species, including superoxide ($^{\bullet}O_2$-) and hydroxyl ($^{\bullet}$OH) radicals, upon UV light irradiation. These radicals play a crucial role in the non-selective mineralization of organic pollutants during photocatalysis on TiO_2 [32]. ZnO also, with its large direct bandgap energy of around 3.37 eV and exciton binding energy of around 60 meV, shows strong UV absorption and effective charge separation [33]. ZnO NPs have the ability to absorb photons of light with energies more than their band gap energy. Therefore, a photo-induced electron moves from the valence band to the conduction band and forms h^+ and e^- on the ZnO surface. The presence of the O atom as an electron acceptor increases the pair of recombinant electron cavities and the production of superoxide radicals. The h^+ and OH^- reaction leads to the formation of hydroxyl radicals [34].

The most significant disadvantage of ZnO and TiO_2 photocatalysts is the fast recombination of electron-hole pairs, lowering the quantum efficiency. The introduction of metallic co-catalysts or the creation of heterojunctions with other metal oxides (such as WO_3, CuO) develops electron-sink effects and advantageous band alignments. Such structural changes improve charge separation, decrease recombination rates, and dramatically enhance overall photocatalytic efficiency [35,36]. Thus, ZnO and TiO_2 can serve as co-catalysts for each other, facilitating charge separation and effectively reducing electron-hole recombination. The preparation of ZnO-TiO_2 nanocomposites may enable new energy levels in the band gap, which can also promote visible light absorption [37].

Zeinali Heris et al. showed 90% degradation of co-amoxiclav using ZnO-TiO_2 nanohybrids under UV light at optimized conditions (pH 11, 2g photocatalyst, 20 mg/L concentration, and 90 min reaction time) [38]. Ge et al. also showed efficient degradation of methyl orange using ZnO/TiO_2 composites, demonstrating their potential as effective photocatalysts for dye removal [39]. Hu et al. showed that ZnO/TiO_2 heterostructure composites achieved enhanced photocatalytic degradation of tetracycline hydrochloride compared with single-component

ZnO or TiO_2, highlighting their potential as efficient photocatalysts for antibiotic wastewater treatment [40].

These results are the pillars of this research, which studies the comparative photocatalytic activity of ZnO, TiO_2, and ZnO-TiO_2 nanocomposites for the photodegradation of pharmaceutical contaminants. ZnO-TiO_2 nanocomposites were synthesized using the chemical precipitation process and systematically characterized using UV-Vis Spectroscopy, FT-IR, XRD, XPS, and FE-SEM to reveal their structural, morphology, and electronic characteristics. Aspirin, Crocin, and Linezolid were chosen as target pollutants due to their extensive consumption by humans and the stability they present in the environment. Additionally, the study explores how critical operating conditions, like pH, temperature, agitation rate, reaction time, and irradiation, influence photocatalytic performance to provide insight into maximizing degradation efficiency. By bringing together new characterization techniques with stringent performance testing, this work aims to contribute towards the development of more efficient and sustainable photocatalytic treatments for pharmaceutical wastewater.

2. Experimental Methodology

2.1. Materials and methods

Analytical grade zinc oxide (CAS no. 1314-13-2; 81.39 g/mol) and titanium oxide (CAS No. 1317-70-0; 79.87 g/mol) were supplied by Sigma Aldrich, USA. Commercial formulations of Aspirin (USV Pvt. Ltd.), Crocin (GSK Healthcare Pvt. Ltd.) and Linezolid (Amigoz Lifesciences) were obtained from a local pharmacy. Deionized water was used for preparation of all solutions.

2.2. Synthesis of ZnO-TiO_2 nanocomposite

ZnO-TiO_2 nanocomposite was synthesized by chemical precipitation method (Fig 1), similar to that reported by Mirda et.al [41] with some modifications. In the experiment, 50 ml of 2% TiO_2 solution was gradually added to 50 ml of 2% ZnO solution. The mixture was magnetically stirred at 600 rpm for 4 hrs. The solution was centrifuged at 4000 rpm for 10 mins after a white precipitate was observed. The pellet was washed thrice with deionized water and dried in an oven at 60°C for 24 hrs to obtain fine nanoparticles.

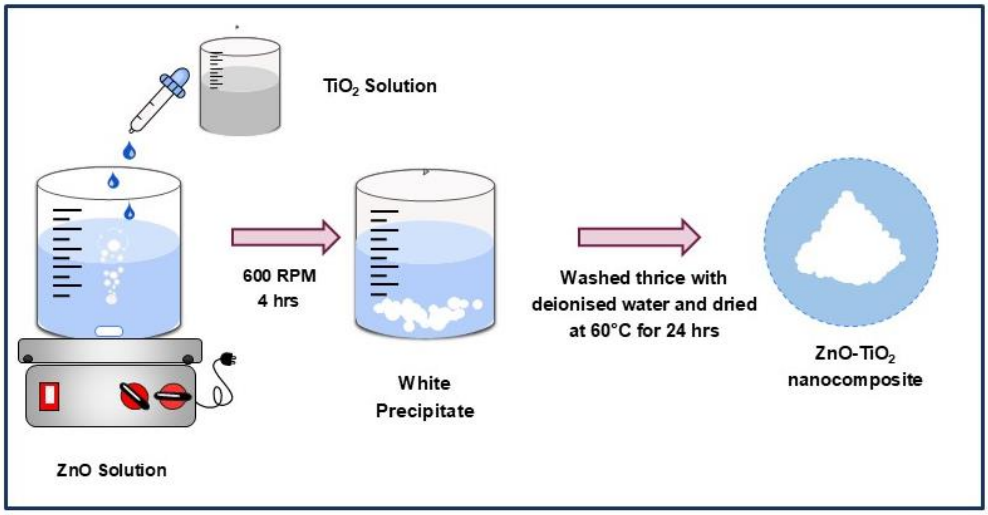

Fig. 1 Schematic representation of the synthesis of ZnO-TiO_2 nanocomposite using chemical precipitation method.

2.3. Characterization techniques

The synthesized compounds were examined by employing different characterization tools to determine their structural, morphological, and optical properties. The particle size, phase purity, and crystallinity were determined using X-ray diffraction (XRD) and measured by the Bruker D8 Advance instrument. A field emission scanning electron microscope (FESEM) (Carl Zeiss Model Supra 55 Germany) was utilized to study the surface morphology of the particles. X-ray photoelectron spectroscopy (XPS) was done by the PHI 5000 VersaProbe III instrument to analyze the composition, electronic state, chemical state, binding energy, and more of the surface region of the material. To investigate the optical properties of the powdered samples, spectra were recorded on an ultraviolet-visible spectrophotometer (Shimadzu model-2600 instrument).

2.4. Preparation of drug solutions

Aspirin, Crocin and Linezolid were separately dissolved in distilled water to create stock solutions of 5 mg/mL, which were then mixed uniformly. The chosen concentration range was based on reported levels of pharmaceuticals and antibiotics in urban wastewater, which typically span from nanograms per litre (ng/L) to milligrams per litre (mg/L) worldwide [42].

2.5. Effect of pH

The effect of pH on drug degradation was examined using ZnO, TiO_2 and ZnO-TiO_2, each at

a concentration of 1 mg/mL. Photodegradation studies were performed under UV irradiation (Micro-Filt India, MFI H 2 x 2 cm, TUV 15 W/G15 T8; Intensity: 53.08 W/cm2) as well as visible light (Philips Master TL-D80 36 W/865). For each trial, nanoparticle suspensions were combined with drug solutions and the reaction mixtures were adjusted to pH 5, 7 and 9. Absorbance was monitored at defined intervals (15, 30, 45, 60, 75 and 90 min) using a UV-Visible Spectrophotometer (Systronics-117). Detection wavelengths were set at 370 nm for Aspirin, 410 nm for Crocin and 590 nm for Linezolid.

2.6. Effect of Temperature

The effect of temperature on drug degradation was examined using ZnO, TiO_2 and ZnO-TiO_2, each at a concentration of 1 mg/mL. Photodegradation studies were performed under UV irradiation (Micro-Filt India, MFI H 2 x 2 cm, TUV 15 W/G15 T8; Intensity: 53.08 W/cm2) as well as visible light (Philips Master TL-D80 36 W/865). For each trial, nanoparticle suspensions were combined with drug solutions and the reaction mixtures were maintained at room temperature, 30°C, 45°C and 60°C. All experiments under visible light were performed at pH 7 under static conditions. Absorbance was monitored at defined intervals (15, 30, 45, 60, 75 and 90 min) using a UV-Visible Spectrophotometer (Systronics-117). Detection wavelengths were set at 370 nm for Aspirin, 410 nm for Crocin and 590 nm for Linezolid.

2.7. Effect of Rate of Agitation

The effect of agitation rate on drug degradation was examined using ZnO, TiO_2 and ZnO-TiO_2, each at a concentration of 1 mg/mL. Photodegradation studies were performed under UV irradiation (Micro-Filt India, MFI H 2 x 2 cm, TUV 15 W/G15 T8; Intensity: 53.08 W/cm2) as well as visible light (Philips Master TL-D80 36 W/865). Nanoparticle suspensions were combined with drug solutions and the reaction mixtures were incubated at agitation speeds of 60, 120 and 180 rpm. All experiments under visible light were performed at pH 7 under static conditions. Absorbance was monitored at defined intervals (15, 30, 45, 60, 75 and 90 min) using a UV-Visible Spectrophotometer (Systronics-117). Detection wavelengths were set at 370 nm for Aspirin, 410 nm for Crocin and 590 nm for Linezolid.

2.8. Evaluating Reusability and Repeatability

The reusability of ZnO-TiO_2 nanocomposite was evaluated by testing their photocatalytic stability and activity across two successive degradation cycles. Aspirin was chosen due to its

optimal degradation in previous studies. A 5 mg/mL stock solution of Aspirin was prepared, and ZnO-TiO_2 nanocomposites were incorporated to reach a final catalyst concentration of 1 mg/mL. The reactions were carried out under the optimized conditions (pH 7, 45°C and 120 rpm) for 45 minutes, and drug degradation was monitored using UV-Vis Spectophotometry. Following each cycle, the catalyst was recovered by centrifugation at 8000 rpm for 10 minutes, rinsed thoroughly with deionized water, and dried at 65°C to remove surface residues. The regenerated photocatalyst was then reused under identical conditions to evaluate performance stability. Changes in degradation efficiency across cycles were analyzed to determine the extent of catalyst deactivation. To gain further insights, structural and surface characteristics of the used catalyst were examined by XPS. Minimal decline in photocatalytic activity over repeated use confirmed the potential of ZnO-TiO_2 nanocomposites as a robust catalyst for pollutant degradation.

2.9. Investigating the Role of Reactive Species in ZnO, TiO_2, ZnO-TiO_2 nanocomposite Photocatalysis by DCPIP assay

To investigate the role of radical scavengers on the photocatalytic activity of ZnO, TiO_2 and ZnO-TiO_2 nanocomposite against Aspirin degradation, experiments were performed by utilizing the 2,6-Dichlorophenolindophenol (DCPIP) assay under optimized conditions. Stock solution of Aspirin (5 mg/ml) was made, and ZnO, TiO_2 and ZnO-TiO_2 nanocomposite were uniformly dispersed at a concentration of 1 mg/ml in respective reaction mixtures. The photocatalytic reaction was carried out under both visible and UV light with optimal conditions such as pH 7, 45°C temperature, and 120 rpm stirring rate for 45 minutes. For identifying the contribution of various reactive species, radical scavengers were added separately in a concentration of 10 mM prior to the reaction start. Isopropanol was employed to scavenge hydroxyl radicals, Vitamin C served as a reactive species scavenger, and EDTA as a hole (h^+) scavenger. Aspirin degradation was traced through the DCPIP assay in which colour loss due to electron transfer was analysed spectrophotometrically at 605 nm. Control runs without scavengers were also done for comparison purposes. The level of inhibition in degradation performance for every scavenger aided in the identification of the major reactive species in the photocatalytic process. These results have a better understanding of ZnO-TiO_2 nanocomposite's photocatalytic processes and their efficacy in degrading pharmaceutical pollutants. The percentage decrease of DCPIP was calculated as follows:

$$\text{Reduction (\%)} = (A_{\text{control}} - A_{\text{sample}})/A_{\text{control}} \times 100$$

2.10. Analysis

The photocatalytic degradation of ZnO-TiO_2 nanocomposite was assessed using an equation that considers the initial and final adsorption rates, denoted as A_0 and A, respectively, along with their corresponding concentrations, C_0 and C. The adsorption rates of ZnO-TiO_2 nanocomposite solutions were measured at specific wavelengths (λ_{max}) of 370 nm, 410 nm, and 590 nm for Aspirin, Crocin, and Linezolid, respectively.

$$\text{Degradation (\%)} = A_0 - A / A_0 \times 100 = C_0 - C / C_0 \times 100$$

2.11 Analysis of Degradation by FTIR Spectroscopy

The photocatalytic degradation of Aspirin was confirmed by Fourier Transform Infrared (FTIR) Spectroscopy. FTIR Spectra of both pure Aspirin and ZnO-TiO_2 treated Aspirin were recorded in the range of 500 - 4500 cm^{-1} using Shimadzu IR Affinity-1. Samples were prepared by ATR Assembly method, and spectra were recorded to compare functional group changes between treated and untreated sample.

3. Result and discussion

3.1 Characterization (UV Spectroscopy of ZnO-TiO_2 nanoparticles)

The light optical characteristics of ZnO-TiO_2 nanocomposite were examined by UV-Visible spectroscopy shown in Fig.2. The structure of ZnO-TiO_2 nanocomposite was confirmed by the UV absorption peak at within the wavelength range of 250-350 nm, indicative of absorption in the ultraviolet region. These peaks are likely attributed to contributions from both the TiO_2 and ZnO components within the nanocomposite.

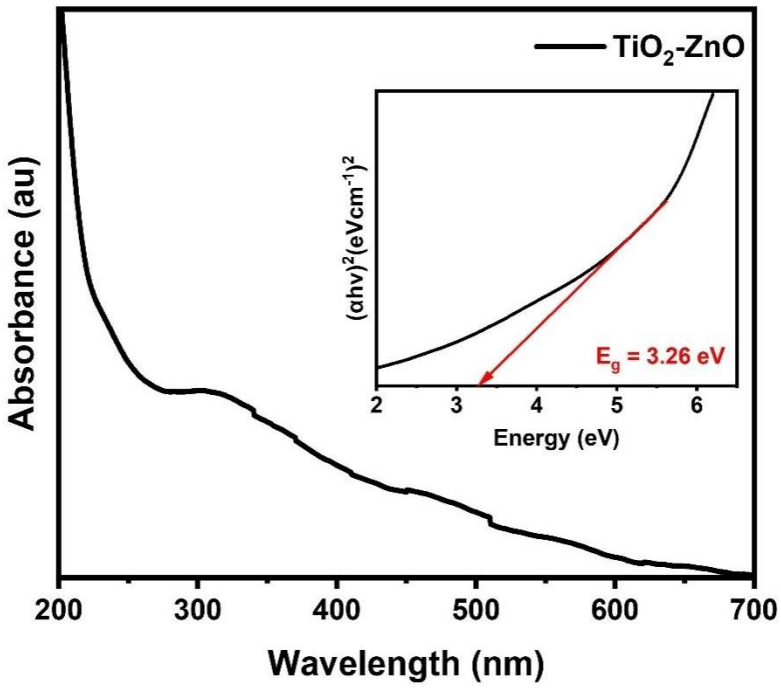

Fig. 2 UV-Vis absorption spectrum of ZnO-TiO_2 nanocomposites, showing their optical properties and characteristic absorption peaks.

The band gap energy of nanocomposite was estimated using the Tauc plot method.

$$(\alpha h\nu)^{\gamma}=A(h\nu-E_g)$$

Where α is the absorption coefficient, h is the plank constant, ν is the photon's frequency, A is the proportionality constant, γ denotes the nature of the electronic transition, and E_g represents the energy gap. γ =1/2 and γ =2 for indirect and direct transitions [43]. Thus, extrapolating the linear region on the abscissa yields the bandgap energy of the nanocomposite. The estimated band gap value of ZnO-TiO_2 nanocomposite is 3.26 eV. This reduction in band gap improved the optical characteristics of the ZnO-TiO_2 nanocomposite, which can be favourable for photocatalytic applications. The energy gradient present at the interface allows the separation of the charge carriers on each part of the heterojunction [44].

3.2 X-Ray Diffraction of ZnO-TiO_2 nanoparticles

XRD technique used to determine the crystal structure, phase purity and particle size. Fig. 3 shows the XRD patterns of ZnO-TiO_2 nanocomposite in which black colour TiO_2 and red ZnO crystal planes. It shows a set of well-defined crystal planes are indexed to the hexagonal wurtzite phase, with lattice constants, a=0.325 nm and b=0.520 nm (JCPDS: 36-1451) to ZnO as well as the diffraction peaks are well assigned to anatase TiO_2 with lattice constants a =

0.378 nm and c = 0.951nm, which are consistent with the values in the standard card (JCPDS 21-1272). So it observed that the diffraction peaks of both anatase TiO_2 and wurtzite ZnO confirm the formation of ZnO-TiO_2nanocomposite.The size was calculated by using Debye-Scherrer's equation $D = 0.9\lambda/\beta\cos\theta$, where λ is the wavelength of the X-ray radiation (λ=0.15406 nm) and β is the line width at the half maximum height [45]. The average nanoparticle size obtained is 23.6 nm [46].

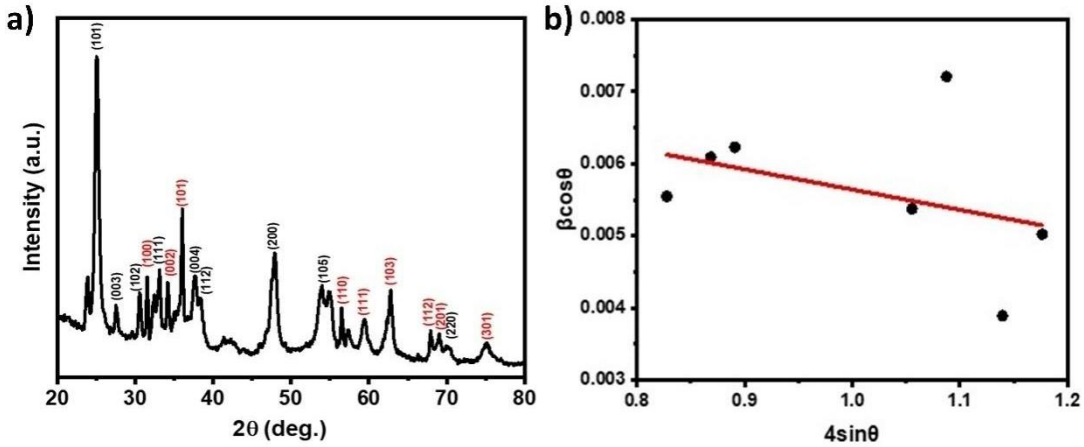

Fig. 3 XRD pattern of ZnO-TiO_2 nanoparticles, displaying their crystalline structure, phase composition, and characteristic diffraction peaks.

The crystallite size and micro strain of the ZnO-TiO_2 nanocomposite are examined from the Williamson–Hall (W-H) equation. The W-H equation for the uniform determination model is given by Shan et.al [47]

$$\beta(hkl)cos\theta(hkl) = k \times \frac{\lambda}{D_V} 4\varepsilon sin\theta(hkl)$$

Where, $\beta(hkl)$ is the FWHM, θ is Bragg's diffraction angle, k is the shape factor, λ is the wavelength of radiation, D_v is the volume-weighted crystallite size, and ε is the lattice strain. The crystallite size of the synthesized ZnO-TiO_2 nanocomposite was found to be 24.7 nm.

3.3 FT-IR Analysis of ZnO-TiO_2 Nanocomposites

The functional groups on the surface acting very crucial role in photocatalytic activity owing to reactions mostly occur on the surface of photocatalyst. Thus, we execute FT-IR analyses on ZnO-TiO_2 nanocomposite with the range of 400-4000 cm^{-1} (Fig. 4). The band observed between 400 and 500 cm^{-1} can be corresponding to stretching vibration of Zn-O bonds. The sharp bands occur at 829 cm^{-1} corresponding to Ti-O-Ti and Ti-O vibrations [48].

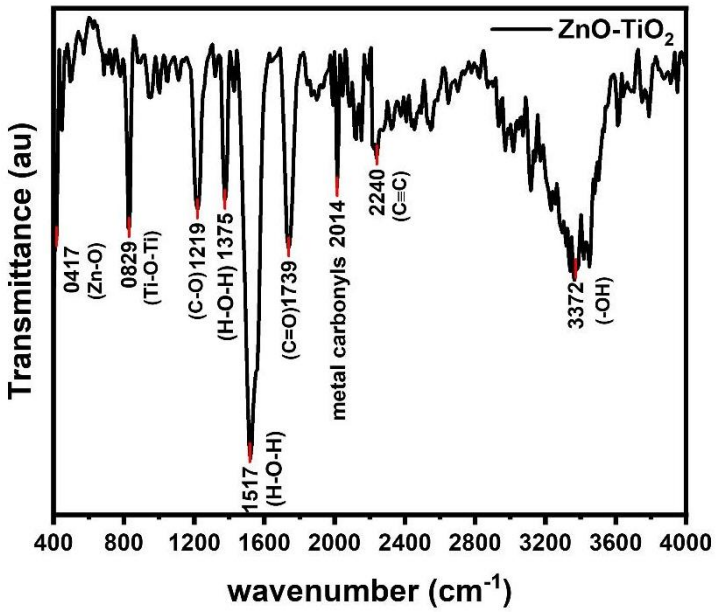

Fig. 4 FTIR spectrum of ZnO-TiO_2 nanocomposites, highlighting the functional groups and molecular vibrations present in the sample.

The bands shown near 1300 to 1500 cm^{-1} is assigned to H-O-H bending vibration mode due to the adsorption of moisture when FT-IR sample disks were prepared in an open-air atmosphere [49].The bands occur at 2014 and 2240 cm^{-1}, related to stretching of metal carbonyls and C≡C, respectively. In addition, the C=O and C-O bending vibrations are assigned to the bands at 1219 and 1739 cm^{-1} respectively. The bands above 3000 cm^{-1} show the existence of a hydroxyl group in the synthesized ZnO-TiO_2 nanocomposite [50].

3.4 XPS Analysis of ZnO-TiO_2 Nanocomposites

The elemental compositions of ZnO-TiO_2 nanocomposite was analysed by XPS, as shown in Fig. 5. In Fig. 5a, XPS survey spectrum specifies that the sample contains Ti, Zn and O elements. The high resolution XPS spectra of Zn 2p, Ti 2p, O 1s and C 1s fitted with Gaussian function is are displayed in Fig. 5b - e. The XPS spectrum of Zn 2p region is shown in Fig. 5b. The two high intense peak positions of Zn $2p_{3/2}$ and Zn $2p_{1/2}$ are located at 1024.6 and 1047.8 eV, respectively, and the binding energy splitting (spin-orbit) Zn $2p_{3/2}$ and Zn$2p_{1/2}$ is 23.2 eV, indicating the Zn species mainly existed as the chemical state of Zn^{2+} [51].

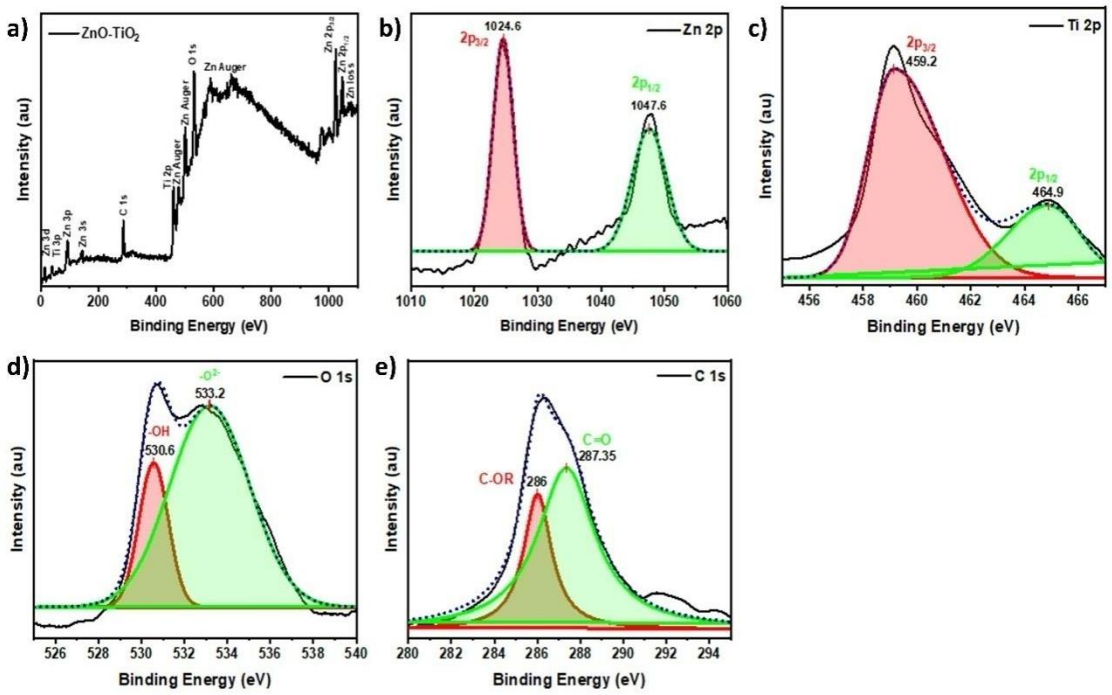

Fig.5 a) XPS b) Zn 2p c) Ti 2p and d) O 1s e) C 1s spectra of ZnO-TiO_2 nanocomposite

In Fig. 5c, the Ti 2p spectra has two peaks centred at 459.2 and 464.9 eV, which are corresponding to Ti $2p_{3/2}$ and $2p_{1/2}$ chemical states of Ti with spin-orbital splitting of photoelectrons is 5.7 eV confirms Ti species mainly existed as the chemical state of Ti^{4+}. The peak at 530.6 eV arises due to O atoms (surface hydroxy group) [52] (Fig. 5d). The appeared to peak at 533.2 eV might have originated due to the presence of oxygen attached to Zn and Ti species. In Fig. 5e represent C 1s spectra indicating to two peaks fitted with gaussian function at 286 and 287.35 eV corresponds to C-OR and C=O species of carbon [53].

3.5 Field Emission Scanning Electron Microscope (FESEM)

Field Emission Scanning Electron Microscopy (FESEM) was employed to investigate the surface morphology of the ZnO-TiO_2 nanocomposite. The micrograph reveals a heterogeneous structure composed of quasi-spherical and irregularly shaped nanoparticles, with evidence of partial agglomeration. The particles appear to be closely packed, forming a network-like morphology with interconnected grain boundaries.

Fig. 6E and F present the corresponding particle size distribution histograms derived from the FESEM images. The histogram in panel 6E shows a unimodal distribution centred around 27 nm, with most particles ranging between 20-35 nm, suggesting a relatively narrow size dispersion. In panel 6F, the distribution is also unimodal but slightly narrower, centred around 24 nm, with the majority of particles falling in the 18-30 nm range.

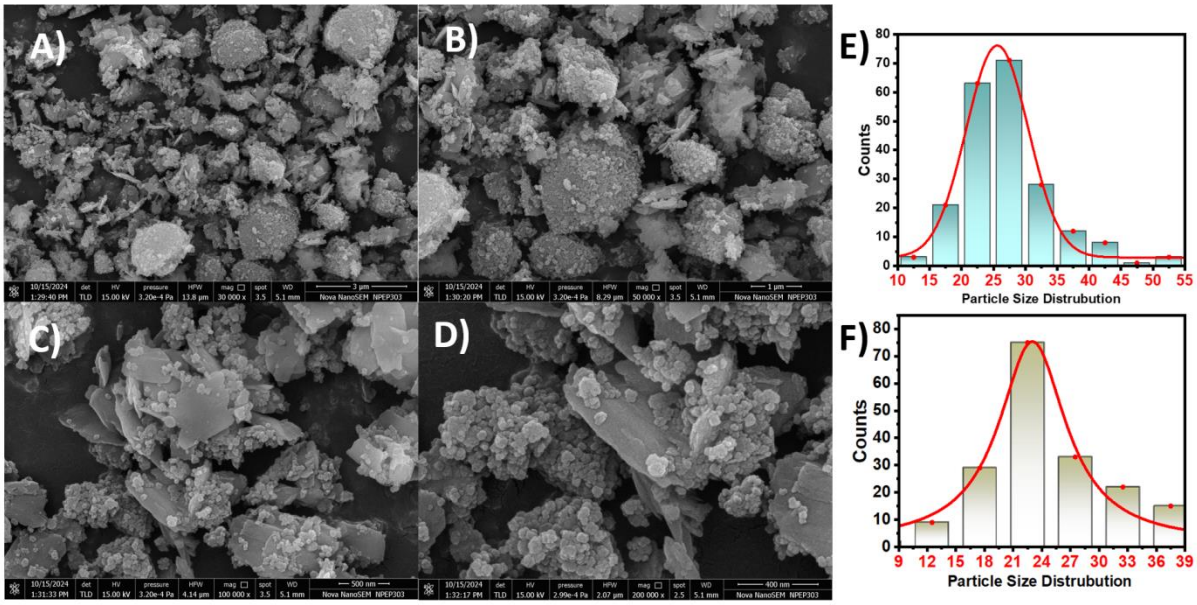

Fig.6 A) to D) FESEM images E) Particle size distribution of fig.6C F) Particle size distribution of fig.6D of ZnO-TiO_2 nanocomposite.

3.6. Photocatalytic Degradation

3.6.1. Effect of pH on degradation of Aspirin, Crocin and Linezolid by ZnO, TiO_2 and ZnO-TiO_2 nanocomposite

Fig. 7 illustrates how pH variations affect the photocatalytic activity of ZnO, TiO_2, and ZnO-TiO_2 nanocomposites. To study this effect, the pH of the drug solutions was adjusted to 5, 7, and 9 using standardized 1N HCl and 1N NaOH solutions. Fig. 7a indicates that among the drugs tested, Linezolid shows the highest degradation 77.43% with ZnO nanoparticles at pH 5, followed by Aspirin, which shows the degradation of 59.61%. For TiO_2 nanoparticles, degradation of the three drugs is constant for all the pH values, between 55% and 60%. Conversely, the greatest degradation for Linezolid occurs at pH 9, with a degradation rate of 62.96% as shown in Fig. 7h. For ZnO-TiO_2 nanocomposites, Fig. 7c shows that the maximum degradation of Linezolid is at pH 5 which is 81%.

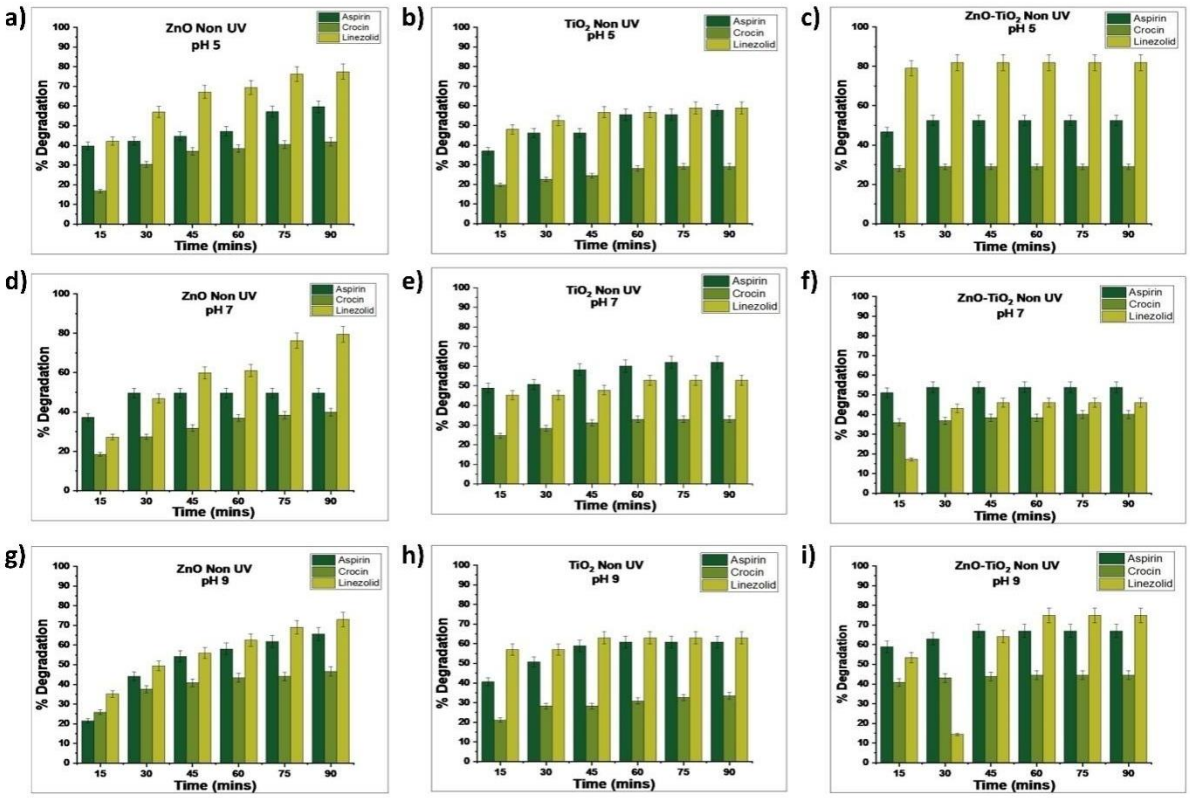

Fig.7 Photocatalytic degradation profiles of Aspirin, Crocin, and Linezolid in the presence of visible light irradiated ZnO, TiO_2, and ZnO-TiO_2 nanocomposites under varying pH conditions. Subfigures a-c represent degradation under acidic conditions (pH 5), d-f under neutral conditions (pH 7), and g-i under basic conditions (pH 9).

Both ZnO and ZnO-TiO_2 nanocomposite exhibit the best performance at pH 5, possibly because of increased surface charge and better adsorption ability for organic pollutants. Acidic environment at this pH favours the effective production of reactive oxygen species (ROS), including hydroxyl radicals, which are essential for the degradation of pollutants [54]. In addition, for ZnO-TiO_2 nanocomposite, the interfacial interaction between the two compounds at pH 5 enables enhanced electron-hole separation, thus improving their photocatalytic activity [55].

Interestingly, TiO_2 shows increased activity at pH 9, which is probably attributed to its negative surface charge, allowing for the adsorption of positively charged species and enhancing degradation efficiency [56]. Under alkaline conditions, TiO_2 also shows increased stability and higher photocatalytic efficiency, which is promoted by favourable surface charge interactions with some pollutants. In addition, TiO_2 characteristics at pH 9 are maximized, which results in the more effective generation of reactive oxygen species (ROS), including hydroxyl radicals

(•OH), thus further improving its photocatalytic activity [57].

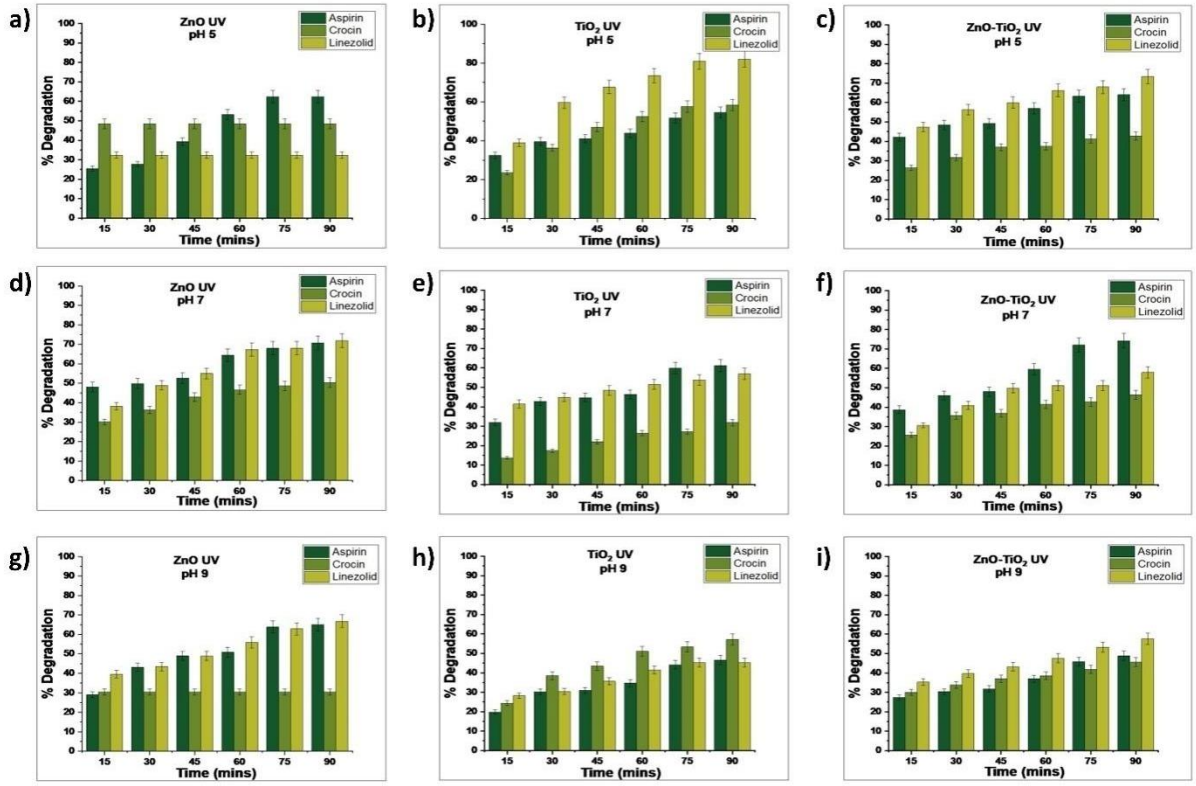

Fig. 8 Photocatalytic degradation profiles of Aspirin, Crocin, and Linezolid in the presence of Irradiated ZnO, TiO_2, and ZnO-TiO_2 nanocomposite under varying pH conditions. Subfigures a-c represent degradation under acidic conditions (pH 5), d-f under neutral conditions (pH 7), and g-i under basic conditions (pH 9).

For UV-irradiated ZnO nanoparticles, the highest degradation was observed in Linezolid at pH 8 with 71.85%, followed in close second by Aspirin at 70.74%. pH 9 also showed high degradation of Linezolid to 66.75%. In UV-irradiated TiO_2 nanoparticles, maximum degradation of Linezolid was found to be at pH 5 with a degradation percentage of 81.99%. ZnO-TiO_2 nanocomposites were also found to exhibit high degradation of Linezolid at pH 5 with an efficiency of degradation of 73.33%. Surprisingly, pH 7 was found effective for the degradation of Aspirin with an efficiency of 74.15%.

The extensive degradation of Linezolid (71.85%) and Aspirin (70.74%) at pH 7 by UV-irradiated ZnO nanoparticles is attributed to favourable surface charge conditions that increase drug adsorption and facilitate efficient generation of reactive oxygen species (ROS) such as hydroxyl radicals. Under both acidic and neutral pH, ZnO's surface supports improved electron-hole separation and ROS generation, resulting in effective photocatalytic activity [58].

In visible light conditions with TiO_2 nanoparticles, pH 9 exhibits increased degradation owing to the negatively charged surface that enhances adsorption of neutral or cationic pollutants. Yet under UV irradiation, TiO_2 produces reactive oxygen species (ROS), and at pH 5, the positively charged surface improves adsorption of negatively charged drug molecules. Furthermore, acidic conditions facilitate greater $^{\bullet}OH$ radical formation, which results in substantially enhanced photocatalytic degradation [59,60].

The maximum degradation of Linezolid at pH 5 which is 73.33% and Aspirin at pH 7 which is 74.15% by ZnO-TiO_2 nanocomposite may be understood on the basis of the synergy of surface charge and reactive oxygen species (ROS) generation. Under pH 5, the composite surface becomes positive, and hence, there is increased adsorption of the negatively charged Linezolid, while ROS generation, especially hydroxyl radicals ($^{\bullet}OH$), is also encouraged, leading to degradation. Conversely, ZnO-TiO_2 nanocomposites at pH 7 are close to their point of zero charge, minimizing electrostatic repulsion and enabling improved adsorption of anionic aspirin. Moreover, ROS generation is maximized under neutral pH, resulting in better degradation [55,59].

3.6.2. Effect of temperature on degradation of Aspirin, Crocin and Linezolid by ZnO, TiO_2 and ZnO-TiO_2 nanocomposite

As shown in Fig. 9a, d, g, and j, the highest degradation with visible light ZnO nanoparticles is observed for Linezolid at room temperature (79.50%) and at 30°C (60.64%). Notably, Aspirin exhibits 58.58% degradation at 60°C. Hermann (1999) and Gogate and Pandit (2004) both highlight those photocatalytic reactions typically have an optimal temperature range for operation, typically between 20°C and 80°C [61,62].

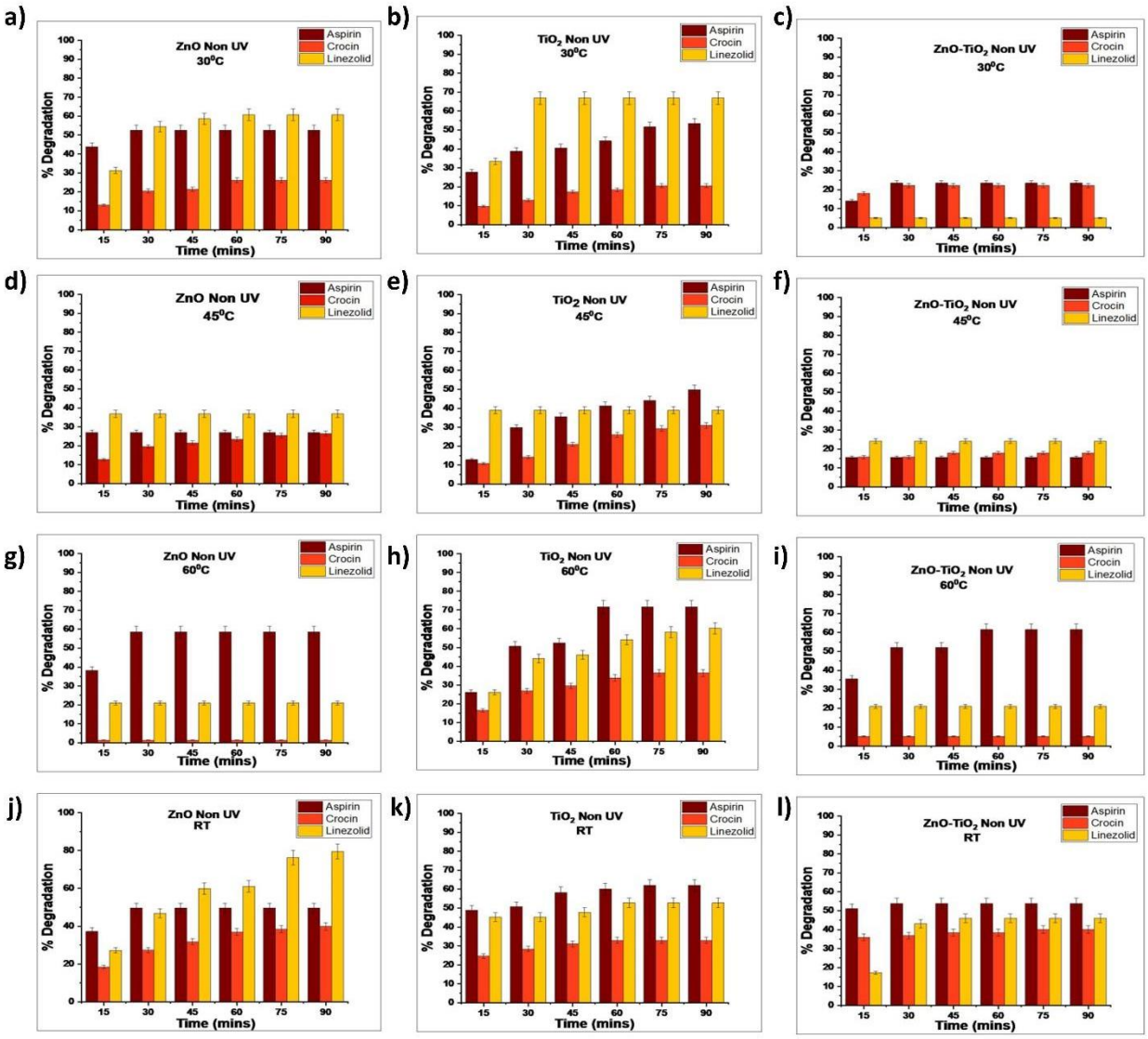

Fig. 9 Photocatalytic degradation profiles of Aspirin, Crocin, and Linezolid in the presence of visible light irradiated ZnO, TiO_2, and ZnO-TiO_2 nanocomposites under varying temperature conditions. Subfigures a-c represent degradation at 30°C, d-f at 45°C, g-i at 60°C and j-l at room temperature(33°C).

Similarly, TiO_2 shows the highest degradation of Linezolid at 66.87% at 30°C and Aspirin at 71.60% at 60°C. This occurs because the photocatalytic activity of TiO_2 nanoparticles relies heavily on factors like surface area, active sites, and charge carriers [63]. Similarly, ZnO-TiO_2 nanocomposites show the highest degradation at 60°C, particularly for Aspirin at 61.52%.

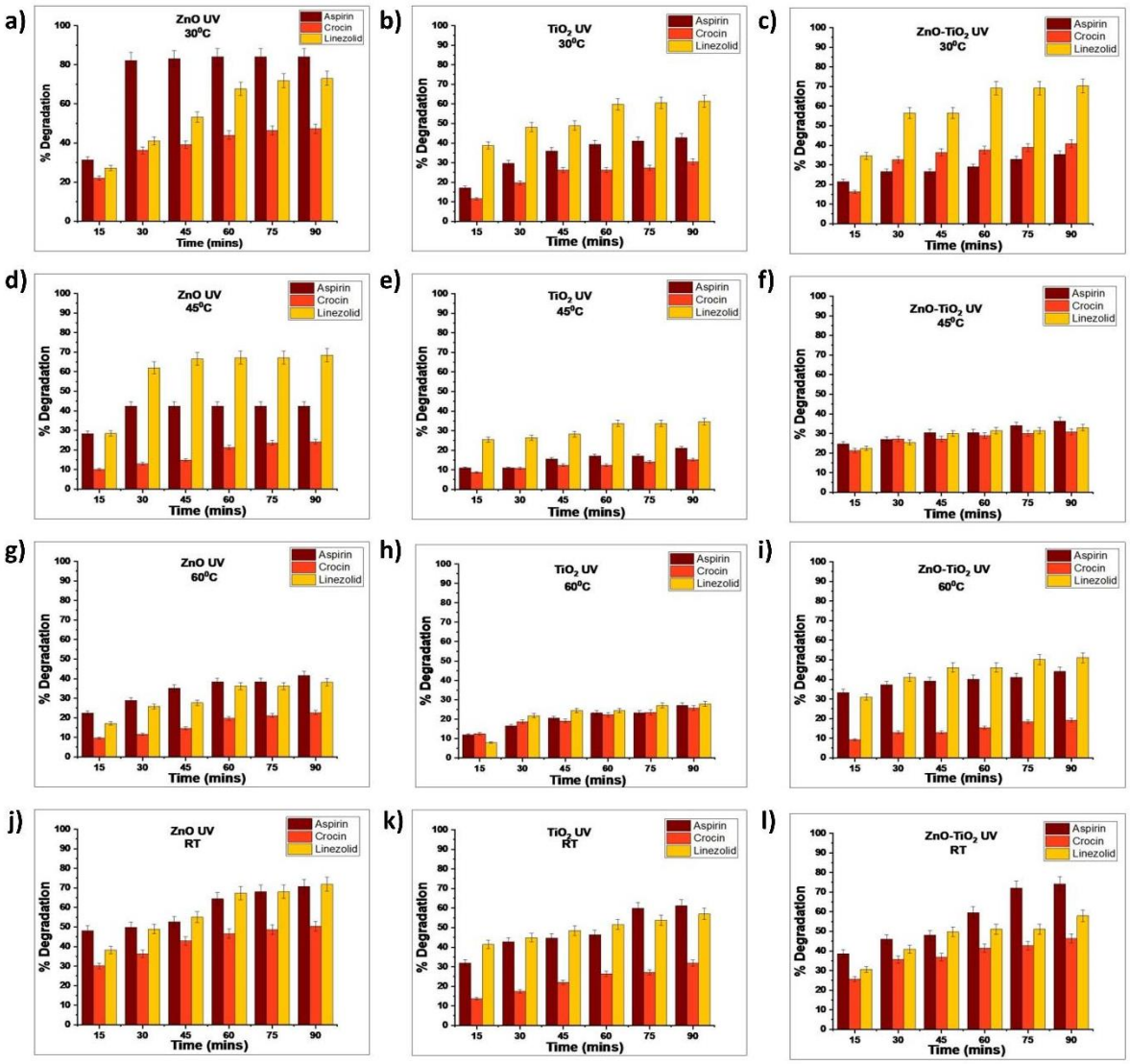

Fig. 10 Photocatalytic degradation profiles of Aspirin, Crocin, and Linezolid in the presence of Irradiated ZnO, TiO_2, and ZnO-TiO_2 nanocomposite under varying temperature conditions. Subfigures a-c represent degradation at 30°C, d-f at 45°C, g-i at 60°C and j-l at room temperature (33°C).

In Fig. 10 a, ZnO nanoparticles display the best photocatalytic degradation efficiency at 30°C, reaching 84.09% degradation of Aspirin and 72.94% for Linezolid. Linezolid also showed significant degradation at 45°C with a rate of 68.46% under the same conditions. TiO_2 nanoparticles had effective photocatalytic activity at 30°C, achieving a degradation efficiency of 61.32% for Linezolid. The ZnO-TiO_2 nanocomposite exhibited the highest degradation efficiency for Linezolid at 30°C (70.26%) and maintained significant activity at 60°C, with 51.09% degradation.

The differences in degradation at various temperatures can be linked to the thermal stability and structural behaviour of the photocatalysts. ZnO shows high activity at 30°C but may suffer photo corrosion at higher temperatures [58]. TiO_2 remains stable with moderate activity due to its resistance to photo corrosion. The ZnO-TiO_2 nanocomposite benefits from both materials, showing efficient charge separation and stable performance across temperatures [64].

3.6.3. Effect of rate of agitation on degradation of Aspirin, Crocin and Linezolid by ZnO, TiO_2 and ZnO-TiO_2 Nanocomposite

As for visible light irradiated nanoparticles in Fig. 11, the rate of agitation at 60 rpm has shown higher degradation for ZnO and TiO_2 whereas 120 rpm shows greater activity for ZnO-TiO_2 nanocomposites. ZnO shows highest degradation at 60 rpm for Aspirin 59.61%. Linezolid also exhibited considerable degradation at 60 rpm 58.92% under the same conditions.

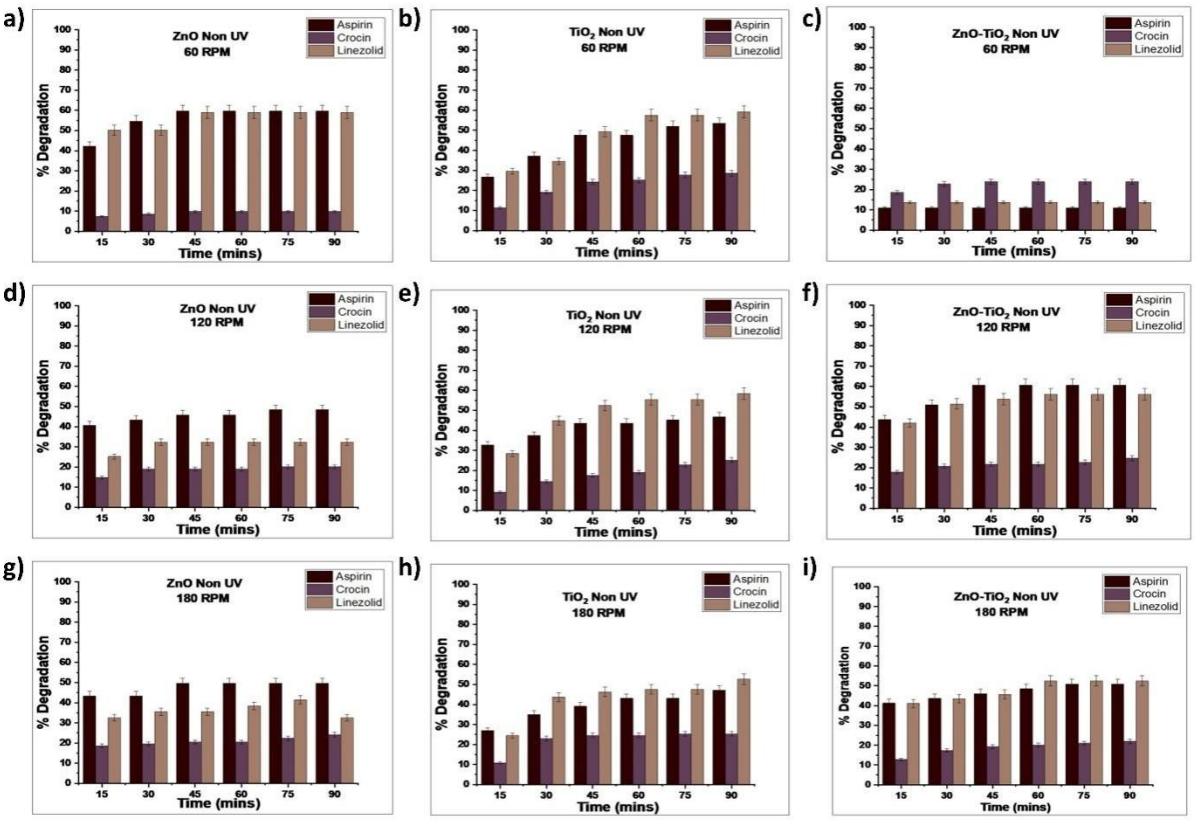

Fig. 11 Photocatalytic degradation profiles of Aspirin, Crocin, and Linezolid in the presence of visible light irradiated ZnO, TiO_2, and ZnO-TiO_2 nanocomposite under varying agitation conditions. Subfigures a-c represent degradation at 60 RPM, d-f at 120 RPM, g-i at 180 RPM.

For TiO_2, while all three speeds demonstrated comparable degradation efficiencies, 60 rpm

showed a slight edge, suggesting it provides optimal conditions for drug interaction with the photocatalyst. It degraded Linezolid up to 59.19%. For ZnO and TiO_2, these results showed nearly identical degradation efficiencies at 60 rpm and 120 rpm, indicating stable performance at these speeds. However, a slight decrease in degradation efficiency was observed at 180 rpm, potentially due to excessive turbulence disrupting the adsorption-desorption equilibrium on the nanoparticle surface. This imbalance may reduce the effective interaction between the photocatalyst and the contaminant, slightly diminishing the reaction efficiency [65].

However, ZnO-TiO_2 nanocomposites demonstrated excellent activity at 120 rpm with highest degradation of Aspirin upto 60.59%, followed by Linezolid 56.04%. The improved photocatalytic activity of ZnO-TiO_2 nanocomposites at a stirring speed of 120 rpm can be linked to better mass transfer and uniform dispersion of nanoparticles. Moderate stirring speeds allow for better interaction between the photocatalyst and pollutant molecules, improving degradation efficiency [66].

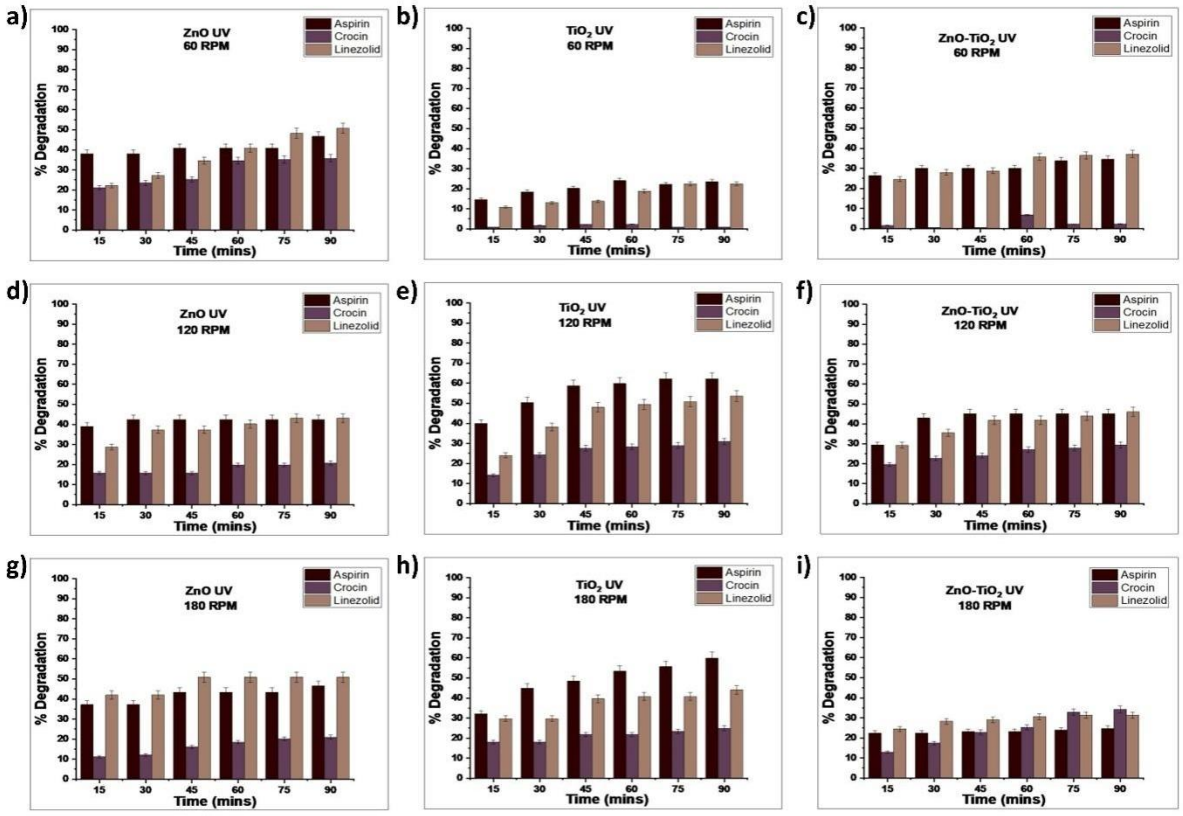

Fig. 12 Photocatalytic degradation profiles of Aspirin, Crocin, and Linezolid in the presence of Irradiated ZnO, TiO_2, and ZnO-TiO_2 nanocomposite under varying agitation conditions. Subfigures a-c represent degradation at 60 RPM, d-f at 120 RPM, g-i at 180 RPM.

The photocatalytic efficiency of irradiated ZnO, TiO_2, and ZnO-TiO_2 nanocomposite was assessed under different agitation conditions. As shown in Fig. 12, all three stirring speeds produced similar degradation trends for irradiated ZnO, with a slight improvement noted at 180 rpm, where Linezolid degradation reached 50.88%. For irradiated TiO_2 nanoparticles, 120 rpm showed a significant increase in activity, achieving degradation efficiencies of 62.16% for Aspirin and 53.65% for Linezolid. The ZnO-TiO_2 nanocomposites also performed best at 120 rpm, with degradation efficiencies of 45.18%, 29.45%, and 46.00% for Aspirin, Crocin, and Linezolid, respectively. These results suggest that moderate stirring (120 rpm) enhances the interaction between the photocatalyst and target molecules by balancing mass transfer and light absorption. Higher agitation rates, like 180 rpm, may lead to excessive turbulence, which could disturb the adsorption-desorption balance on the nanoparticle surface and slightly reduce photocatalytic efficiency.

A comparative evaluation of photocatalytic degradation under visible and UV light revealed pronounced differences in efficiency depending on both irradiation source and catalyst composition (Table1 and 2). Overall, UV irradiation consistently showed significantly higher degradation efficiencies than visible light for all three pharmaceutical drugs, confirming the stronger photoactivation of ZnO, TiO_2, and ZnO-TiO_2 under UV exposure. Under visible light, degradation was moderate and strongly dependent on optimized pH and agitation, with the highest removal observed for Linezolid using the ZnO-TiO_2 nanocomposite (81%). In contrast, UV light markedly enhanced photocatalytic performance, particularly for Aspirin and Linezolid, with maximum degradation reaching 84.09% for Aspirin (ZnO) and 81.99% for Linezolid (TiO_2) under optimized conditions. Neutral to mildly acidic pH combined with moderate to high agitation emerged as common optimal parameters under UV irradiation, whereas visible light driven degradation generally required narrower operational windows. Notably, the ZnO-TiO_2 nanocomposite showed improved activity under both light sources, demonstrating a significant synergistic effect, while the overall enhancement under UV light underscores the critical role of irradiation energy in driving efficient pharmaceutical pollutant degradation. In the above photocatalysis study pH 5, Temp 30℃ and 60°C (Visible light and UV respectively) and 120 rpm for 90 minutes were selected as an economically feasible optimised condition for further analysis of stability reusability study. Among the tested drugs, the degradation efficiency for linezolid and aspirin was higher compared to crocin. Further comparison between linezolid and aspirin showed nearly similar degradation efficiencies. Aspirin was selected for further analysis as it is more widely used than linezolid, being an over-the-counter drug with analgesic and cardioprotective applications. Its broad environmental

presence and stability make it a common pollutant in water and hence, it should be removed from the waste effluent before discharging it in the receiving river water.

Table 1 Comparison of the Photocatalytic Efficiency of ZnO, TiO_2 Nanoparticles and ZnO-TiO_2 Nanocomposites in Degrading Pharmaceutical drugs and its optimised condition under visible light.

NPs	Drug	pH Best %	Temperature Best %	RPM Best %	Overall, Max degradation	Optimum conditions
ZnO	***Aspirin***	pH 5 59.61%	60°C 58.58%	60 RPM 59.61%	59.61%	pH 5, 60°C and 60 RPM
	Crocin	pH 7 Max 45-48%	RT 45%	180 RPM 25%	48%	pH 7, RT and 180 RPM
	Linezolid	pH 5 77.43%	RT 79.50%	60 RPM 58.92%	79.5%	pH 5, RT, and 60 RPM
TiO_2	***Aspirin***	Constant for all pH range 55% and 60%	60°C 71.6%	60 RPM optimal	71.6%	pH 7, 60°C and 60 RPM
	Crocin		RT 40%		60%	pH 7, RT and 60 RPM
	Linezolid	Conversely percentage at pH 9 62.96%	30°C 66.87%		66.87%	pH 9, 30°C and 60 RPM
ZnO-TiO_2	***Aspirin***	pH 5 55-60%	60°C 61.52%	60 RPM 60.59%	61.52%	pH 5, 60°C and 60 RPM
	Crocin	30–45% increase with pH	RT 35-40%	120 RPM 25%	35-40%	pH 7, RT and 120 RPM
	Linezolid	pH 5 81%	RT 47%	120 RPM 56.04%	81%	pH 5, RT and 120 RPM

Table 2 Comparison of the Photocatalytic Efficiency of ZnO, TiO_2 Nanoparticles and ZnO-TiO_2 Nanocomposites in Degrading Pharmaceutical drugs and its optimised condition under UV light.

NPs	Drug	pH Best %	Temperature Best %	RPM Best %	Overall, Max degradation	Optimum conditions
ZnO	***Aspirin***	pH 7 70.74%	30°C, 84.09%	180 RPM 40-45%	84.09%	pH 7, 30°C and 180 RPM
	Crocin	pH 7 50-55%	RT 50%	60 RPM 35%	50%	pH 7, RT and 60 RPM
	Linezolid	pH 7 71.85%	30°C 72.94%	180 RPM 50.88%	72.94%	pH 7, 30°C and 180 RPM
TiO_2	***Aspirin***	pH 7 60%	RT 60%	120 rpm 62.16%	62.16%	pH 7, RT and 120 rpm
	Crocin	pH 5 60%	RT 30%	120 RPM 25%	60%	pH 5, RT and 120 RPM
	Linezolid	pH 5 81.99%.	30°C, 61.32%	120 RPM 53.65%	81.99%	pH 5, 30°C and 120 RPM
ZnO-TiO_2	***Aspirin***	pH 74.15%.	RT 70%	120 RPM 45.18%,	74.15%	pH 7, RT and 120 RPM
	Crocin	pH 7 45%	RT 40-45%	120 RPM 29.45%,	45%	pH 7, RT and 120 RPM
	Linezolid	pH 5 73.33%	30°C 70.26%	120 RPM 46%	73.33%	pH 7, 30°C and 120 RPM

3.7. FT-IR analysis for confirmation of structural changes in Aspirin treated with ZnO-TiO_2 nanocomposite

FTIR analysis of aspirin treated with ZnO-TiO_2 nanocomposite, exhibits pronounced changes

consistent with surface-mediated interaction and partial decomposition. The ester C=O stretching band, originally sharp around 1684 cm^{-1} in pure aspirin, is notably diminished and broadens toward ~1612 cm^{-1} indicating disruption of the acetyl group via hydrolysis or strong hydrogen bonding on the oxide surface [48]. At ~3394 cm^{-1}, a broad O–H stretching band becomes apparent, characteristic of surface hydroxyl groups or water adsorbed by TiO_2 and ZnO matrices, as commonly reported in composite studies [49]. A new stretching vibration at ~2363 cm^{-1} corresponds to CO_2-like or carbonate species, suggesting oxidative breakdown products adsorbed on the metal oxide surface a hallmark of aspirin mineralization under photocatalytic action [50].

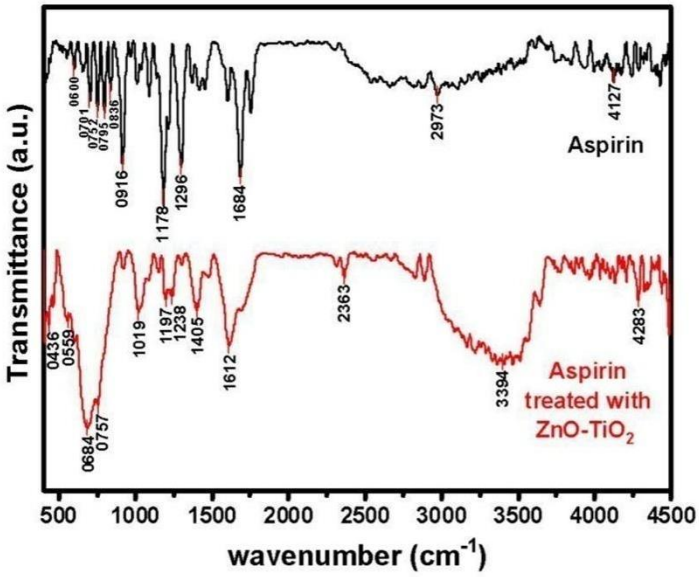

Fig. 13 Comparison of FTIR Spectra of Pure Aspirin and ZnO-TiO_2 nanocomposite Treated Aspirin

Additionally, the appearance of vibrational features in the low-frequency range (~436-559 cm^{-1}) aligns with metal-oxygen bonds (Zn-O and Ti-O) intrinsic to ZnO-TiO_2 composites [49]. Collectively, these spectral signatures reinforce the conclusion that aspirin undergoes surface adsorption and partial hydrolysis when in contact with ZnO-TiO_2, forming hydroxyl and carbonate species, altering functional group vibrations, and demonstrating the intrinsic metal-oxide bonding environment.

3.8. Reusability and Stability of ZnO NPs, TiO_2 NPs and ZnO-TiO_2 nanocomposite for photocatalysis activity

Degradation efficiency after 2 cycles of ZnO NPs, TiO_2 NPs and ZnO-TiO_2 Nanocomposite against the drug Aspirin at pH 7, Temp 45℃ and 120 rpm for 45 minutes was checked. ZnO-TiO_2 Nanocomposites demonstrated a consistent trend in photocatalytic degradation efficiency of the drug aspirin over successive reuse cycles. As shown in Table 3, the initial degradation efficiency in the first cycle was 61.18%, which dropped slightly to 60.29% in the second cycle. This slow decline shows minimal loss in activity. It highlights the good stability and effective reusability of the nanoparticles, which reinforces their potential for real-world use in degrading pharmaceutical contaminants.

Table 3: Degradation efficiency after 2 cycles of ZnO NPs, TiO_2 NPs and ZnO-TiO_2 Nanocomposite against the drug Aspirin at pH 7, Temp 45℃ and 120 rpm for 45 minutes.

NPs	First Cycle	Second Cycle
ZnO NPs	12.11%	71.30%
TiO_2 NPs	34.96%	66.74%
ZnO-TiO_2 Nanocomposites	61.18%	60.29%

Recent studies have validated the reusability of ZnO-TiO_2 nanocomposites as effective photocatalysts for degrading organic pollutants. It is reported that the green-synthesized nanocomposite achieved a decolorization efficiency of 90.2% in the second cycle and 85.5% in the third cycle for methylene blue dye under solar irradiation.The slight reduction in efficiency was attributed to minor catalyst loss and surface fouling by degradation by-products, demonstrating the material's strong potential for repeated use in photocatalytic applications [67].

Similarly, an article in Catalysts described the synthesis of a Cu-ZnO/TiO_2 nanocomposite via a sonochemical method, which achieved complete degradation of Congo red dye within 20 minutes under sunlight and retained its photocatalytic efficiency over five consecutive cycles. These findings highlight the strong reusability and practical potential of ZnO-TiO_2-based photocatalysts in wastewater treatment applications [68]. Our study aligns with these reports, further demonstrating the excellent reusability and photocatalytic efficiency of ZnO-TiO_2 nanocomposites for organic pollutant degradation.

3.9. Investigating the Role of Reactive Species in the Photocatalysis of ZnO, TiO_2, and ZnO-TiO_2 nanocomposite by the DCPIP Assay

In this study, the generation of reactive oxygen species (ROS) by ZnO NPs and their scavenging activity were evaluated using DCPIP. The degradation efficiencies of different experimental groups involved in scavenging were assessed under controlled conditions - pH 7, 45°C, and 120 rpm over a 45-minute period, using the drug Aspirin as the target pollutant.

Table 4: Effect of radical scavengers on linezolid degradation by ZnO NPs, TiO_2 NPs and ZnO-TiO_2 nanocomposite using DCPIP Assay

NPs	**NPs + DCPIP**	**NPs + Drug + DCPIP**	**Vitamin C $O_2^{\bullet-}$**	**Isopropanol ●OH**	**EDTA H+**
ZnO NPs	9.43%	10%	34.37%	45.23%	39.39%
TiO_2 NPs	10.52%	22.01%	36.92%	9.90%	14.68%
ZnO-TiO_2 Nanocomposite	8.07%	46.55%	45.45%	27.58%	41.30%

The role of reactive species in the photocatalytic degradation mechanism of ZnO nanoparticles was evaluated using specific scavengers: Vitamin C for superoxide radicals ($O_2^{\bullet-}$), isopropanol for hydroxyl radicals ($^{\bullet}OH$), and EDTA for photogenerated holes (h^+). The corresponding degradation efficiencies were 34.37%, 45.23%, and 39.39%, respectively Table 4. Although the degradation was lowest in the presence of Vitamin C, the noticeable reduction with isopropanol indicates that hydroxyl radicals are significantly involved in the photocatalytic process. However, the relatively higher degradation in the presence of isopropanol, compared to TiO_2-based systems, suggests that ZnO nanoparticles follow a more distributed mechanism, with all three reactive species $^{\bullet}OH$, $O_2^{\bullet-}$, and h^+ contributing to pollutant breakdown. This is consistent with literature reports, which show that while hydroxyl radicals play a key role, superoxide radicals and photogenerated holes also significantly influence the photocatalytic activity of ZnO. A study published in RSC Advances examined the photocatalytic degradation of methylene blue (MB) using hierarchical ZnO flower structures. The researchers employed

scavengers to identify the active species involved: benzoquinone (BQ) for superoxide radicals, isopropanol (IPA) for hydroxyl radicals, and EDTA for holes. The degradation efficiency decreased significantly in the presence of each scavenger, indicating that all three species contribute to the photocatalytic process. Notably, the presence of BQ led to the most substantial decrease, suggesting a dominant role for superoxide radicals in this system [69].

Several independent scavenger-studies on ZnO photocatalysts converge on the same conclusion: hydroxyl radicals (•OH) are the chief oxidising species that drive the degradation of organic pollutants. Alam et al. demonstrated that introducing isopropanol (an •OH quencher) to rare-earth-doped ZnO cut dye removal by roughly one-half, whereas hole (EDTA) and superoxide (benzoquinone) scavengers produced only minor inhibition, marking •OH as the dominant actor [70].

The role of reactive species in the photocatalytic degradation by TiO_2 nanoparticles was assessed using scavengers-Vitamin C (for $O_2^{\bullet -}$), isopropanol (for •OH), and EDTA (for h^+) Table 4. The degradation efficiencies recorded were 36.92% with Vitamin C, 9.90% with isopropanol, and 14.68% with EDTA. The notable drop in degradation with the addition of isopropanol suggests that hydroxyl radicals (•OH) play a major role in the photocatalytic process. This finding matches earlier studies, such as those by Zhou et al., who noted significant inhibition of pharmaceutical degradation by TiO_2 in the presence of isopropanol, highlighting the importance of •OH radicals in TiO_2-mediated photocatalysis [71].

The photocatalytic degradation mechanism of ZnO-TiO_2 nanocomposites was evaluated using specific radical scavengers: Vitamin C for superoxide radicals ($O^{2\bullet -}$), isopropanol for hydroxyl radicals (•OH), and EDTA for photogenerated holes (h^+). The degradation efficiencies observed were 45.45% with Vitamin C, 27.58% with isopropanol, and 41.30% with EDTA Table 4.

The most significant reduction in degradation efficiency occurred with isopropanol, suggesting that hydroxyl radicals play a crucial role in the photocatalytic process. However, the significant decreases seen with EDTA and Vitamin C indicate that photogenerated holes and superoxide radicals also contribute importantly to overall photocatalytic activity. This suggests a multi-radical mechanism where •OH, h^+, and $O_2^{\bullet -}$ work together, likely due to better charge separation and interfacial interactions within the ZnO-TiO_2 nanocomposite structure.

These findings are consistent with previous studies. For example, research by Zhang et al. showed that in TiO_2-based systems, the addition of isopropanol significantly reduced the

photocatalytic degradation of pharmaceuticals, reinforcing the critical role of hydroxyl radicals in the process. Similarly, a study by Kumar et al. found that isopropanol addition led to nearly 50% suppression of degradation efficiency, emphasizing the importance of hydroxyl radicals in photocatalytic action [72]. Overall, these studies support the conclusion that hydroxyl radicals are the primary reactive species in the photocatalytic degradation of ZnO-TiO_2 nanocomposites, with superoxide radicals and photogenerated holes also playing significant roles.

3.10. XPS Analysis of ZnO-TiO_2 Nanocomposite after two cycles

XPS analysis as shown in the C 1s spectrum (Fig. 14D), the dominant peaks at 284.0-284.3 eV correspond to C-C/C-H bonds from residual hydrocarbon species or adventitious carbon [73]. Notably, a peak at 285.65 eV is attributed to C=O groups, typically present in alcohol or ester functionalities. The absence of strong signals around 288.5 eV corresponding to O-C=O (carboxylic or ester carbon) suggests possible cleavage of the ester bond in aspirin. Additionally, the O 1s spectrum (Fig.14E) shows a high-binding energy peak at 533.69 eV, which may be associated with hydroxylated degradation products, such as salicylic acid or acetic acid. The diminished intensity or absence of characteristic ester carbon and oxygen peaks indicates that aspirin molecules undergo hydrolysis or oxidative degradation on the oxide surface [74].

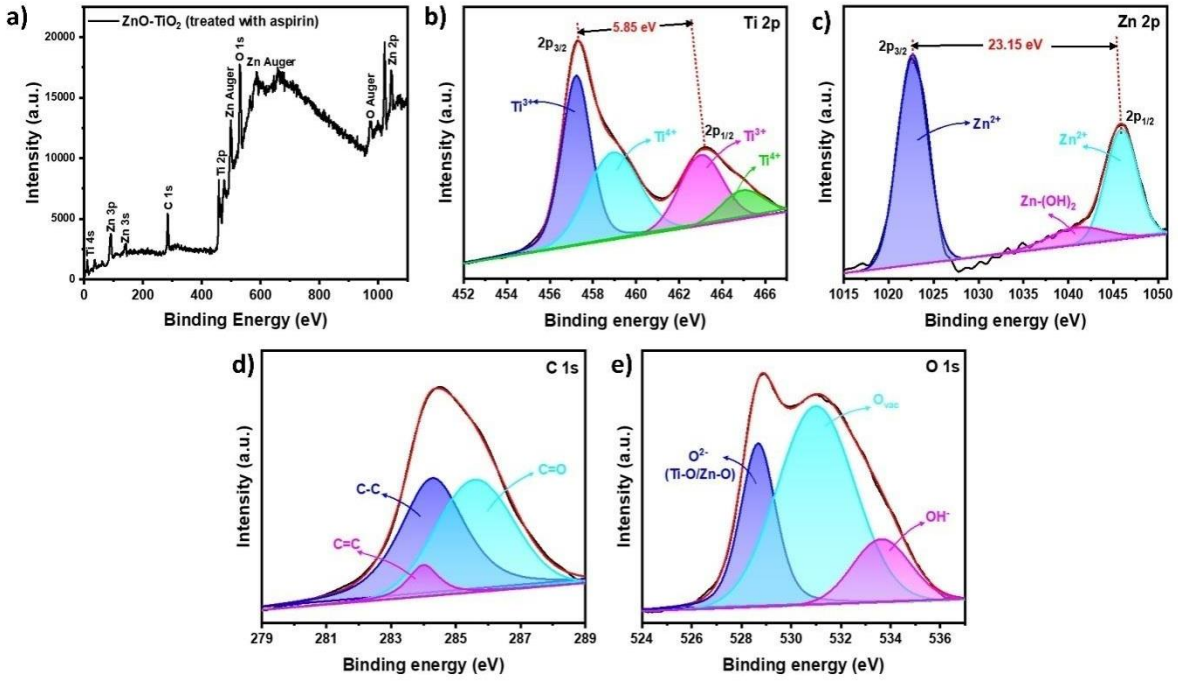

Fig. 14 a) XPS spectra B) Ti 2p C) Zn 2p D) C1s E) O1s spectra of ZnO-TiO_2 nanocomposite after treatment with Aspirin.

Furthermore, the emergence of Ti^{3+} states (457.27 and 465.08 eV) and enhanced oxygen vacancy signals (530.97 eV) in the Ti 2p and O 1s regions imply that the semiconductor surface may actively participate in redox processes, facilitating the breakdown of pharmaceutical molecules under ambient or photochemical conditions [75].

Table 5 Photocatalytic degradation reaction ZnO NPs, TiO_2 NPs and ZnO-TiO_2 nanocomposites under UV and Visible light

NPs	***Photocatalytic degradation reaction***	***ROS involved***	***Ref.***
ZnO	Drug + ZnO + hν + O_2 + H_2O → Degraded products + CO_2 + H_2O	$O_2{\cdot}^-$ drive degradation; H_2O_2 acts as secondary oxidant	[76]
TiO_2	Drug + TiO_2 + hν + O_2 + H_2O → Degraded products + CO_2 + H_2O	$\cdot O_2{\cdot}^-$ oxidize drug molecules h^+ contributes to direct oxidation	[77-79]
ZnO-TiO_2	ZnO–TiO_2 + hν + O_2 + H_2O → $\cdot OH$ + $O_2{\cdot}^-$ Drug + ($\cdot OH$ + $O_2{\cdot}^-$) → Degraded products + CO_2 + H_2O	Enhanced $\cdot OH$ and $O_2{\cdot}^-$ production due to suppressed recombination yields highest degradation efficiency	[80]

When exposed to light, both TiO_2 and ZnO, when utilized as individual particles, will absorb incoming light energy, producing an electron-hole pair in the conduction band and valence band of each particle, respectively. Photogenerated electrons from each particle react with dissolved O_2 forming a superoxide radical anion (O_2-) and holes produced in the valence band of TiO_2 oxidize water/hydroxyl groups adsorbed onto the surface of the TiO_2 to produce highly reactive hydroxyl radicals ($^{\bullet}OH$). These reactive oxygen species (ROS) will initiate and propagate organic waste degradation leading to smaller intermediates releasing CO_2 and H_2O at the end of degradation (Table5).

In ZnO-TiO_2 composite, the photoexcitation of both semiconductors occurs simultaneously because of similar structures. The band alignments are such that the electrons generated in the conduction bands of ZnO can easily be transferred to the conduction bands of TiO_2 and likewise the holes generated in TiO_2 can easily migrate to hydrogen anion sites in ZnO. The transfer of electrons and holes at the junction between the two semiconductors significantly reduces the chance of electron-hole recombination, which allows for the more efficient separation of

electrons and holes. This more efficient separation of charge allows for the more effective generation of superoxide and hydroxyl radicals compared to the individual processes. The increased generation of reactive species will cause enhanced rates of degradation of organic waste resulting in higher photocatalytic activity of ZnO-TiO_2 composites.

Conclusion

In this research, ZnO, TiO_2, and ZnO-TiO_2 nanocomposite were tested for their photocatalytic activity against pharmaceutical pollutants, namely aspirin and linezolid. ZnO and TiO_2 were purchased from commercial sources, while the composite was prepared using chemical precipitation with a bandgap energy of 3.26 eV. Under both UV and Visible light irradiation, the ZnO-TiO_2 composite showed equal or slightly better performance compared to the pure oxides, especially at pH 5 and 60 °C. Maximum degradation was found at 120 rpm with around 65-70% and 75-80% degradation efficiencies of aspirin and linezolid, respectively. The reaction conditions affected each catalyst individually; ZnO was most effective at pH 5 in the absence of UV, whereas TiO_2 had a better activity at pH 5 and 60 °C under UV. The composite was more effective at lower agitation speeds in the presence of UV but was comparatively less efficient under thermal fluctuation. Mechanistic experiments identified hydroxyl radicals ($^{\bullet}OH$) as the prevalent species for ZnO and TiO_2, while ZnO-TiO_2 composite exhibited a multi-radical mechanism with $^{\bullet}OH$, h^{+}, and $O_2^{\bullet-}$, indicating synergistic promotion in ROS formation. FTIR also verified effective degradation of aspirin. Additionally, reusability assay indicated that the composite maintained its catalytic efficacy over several cycles, suggesting structural stability and scope for repeated use. While additional mechanistic validation is called for, the ZnO-TiO_2 composite appears to be an effective photocatalyst for degradation of pharmaceuticals during water treatment processes.

Conflict of Interest

The authors declare that they have no competing interests.

Data Availability

The data supporting this study are available within the article and its Electronic Supplementary Information (ESI). Additional raw data are available from the corresponding author upon reasonable request.

Acknowledgement

The authors acknowledge the Department of Biotechnology, MES Abasaheb Garware College (Autonomous), and the Department of Physics, Fergusson College (Autonomous), Savitribai Phule Pune University, Pune, India, for laboratory support, and the Central Instrumentation Facility (CIF), SPPU, for sample analysis.

References:

1. Marsalek, J. Pharmaceuticals and Personal Care Products in Canadian Urban Waters; *Springer: Dordrecht*, **2008**; Chapter 12. https://doi.org/10.1007/978-1-4020-6795-2_12
2. Van Boeckel, T. P.; Gandra, S.; Laxminarayan, R. *Lancet Infect. Dis*. **2014**, 14, 742–750. https://doi.org/10.1016/S1473-3099(14)70780-7
3. Ternes, T. A. TrAC, *Trends Anal. Chem.* **2001,** 20, 419–434. https://doi.org/10.1016/S0165-9936(01)00078-4
4. Zrnčić, M.; Gros, M.; Petrović, M. *Chemosphere* **2014,** 99, 224–232. https://doi.org/10.1016/j.chemosphere.2013.10.091
5. Kidd, K. A.; Blanchfield, P. J.; Mills, K. H. *Proc. Natl. Acad. Sci. U.S.A.* **2007**, 104, 8897–8901. https://doi.org/10.1073/pnas.0609568104
6. Bottoni, P.; Caroli, S.; Caracciolo, A. B. *Toxicol. Environ. Chem.* **2010**, 92, 549–565. https://doi.org/10.1080/02772241003614320
7. Aus der Beek, T.; Weber, F. A.; Küster, A. *Environ. Toxicol. Chem.* **2016,** 35, 823–835. https://doi.org/10.1002/etc.3339
8. Mutiyar, P. K.; Gupta, S. K.; Mittal, A. K. *Ecotoxicol. Environ. Saf.* **2018**, 148, 207–215. https://doi.org/10.1016/j.ecoenv.2017.12.041
9. Gopal, C. M.; Bhat, K.; Ramaswamy, B. R. *J. Environ. Chem. Eng.* **2021**, 9, 105610. https://doi.org/10.1016/j.jece.2021.105610
10. Jukosky, J. A.; Watzin, M. C.; Leiter, J. C. *Aquat. Toxicol*. **2008,** 88, 42–50. https://doi.org/10.1016/j.aquatox.2007.11.012
11. Péan, S.; Daouk, T.; Vignet, C. *Neurotoxicol. Teratol.* **2013,** 39, 31–38. https://doi.org/10.1016/j.ntt.2013.07.001
12. Gonzalez, S. T.; Remick, D.; Colwill, R. M. *Neurotoxicology* **2016,** 53, 173–180. https://doi.org/10.1016/j.neuro.2015.12.018

13. Cizmas, L.; Sharma, V. K.; McDonald, T. *J. Environ. Chem. Lett*. 2015, 13, 345–355. https://doi.org/10.1007/s10311-015-0524-4
14. Asheghmoalla, M.; Mehrvar, M. *Water* **2024,** 16, 2086. https://doi.org/10.3390/w16152086
15. Rosli, F. A.; Ahmad, H.; Jumbri, K. R. *Soc. Open Sci.* **2021,** 8, 201076. https://doi.org/10.1098/rsos.201076
16. Casas, M. E.; Chhetri, R. K.; Ooi, G. *Water Res.* **2015,** 83, 240–250. https://doi.org/10.1016/j.watres.2015.06.042
17. Dolar, D.; Kosutić, K.; Asperger, D. *Water Air Soil Pollut.* **2012,** 223, 5905–5916. https://doi.org/10.1007/s11270-012-1377-0
18. Subedi, B.; Balakrishna, K.; Sinha, R. *J. Environ. Chem. Eng.* **2015,** 3, 2880–2886. https://doi.org/10.1016/j.jece.2015.09.031
19. Al-Mashaqbeh, O.; Alsalhi, L.; Salaymeh, L. *Sci. Total Environ*. **2024**, 912, 173634. https://doi.org/10.1016/j.scitotenv.2024.173634
20. Iyer, A. M.; Karande, A. V.; Gogate, P. R. *Processes* **2025**, 13, 1191. https://doi.org/10.3390/pr13041191
21. de Ilurdoz, M. S.; Sadhwani, J. J.; Reboso, J. V. *J. Water Process Eng*. **2022**, 45, 102474. https://doi.org/10.1016/j.jwpe.2021.102474
22. Ternes, T. A. *Water Res.* **1998,** 32, 3245–3260. https://doi.org/10.1016/S0043-1354(98)00099-2
23. Hübner, U.; Spahr, S.; Lutze, H. *Heliyon* **2024,** 10, e30402. https://doi.org/10.1016/j.heliyon.2024.e30402
24. Buxton, G. V.; Greenstock, C. L.; Helman, W. P. *J. Phys. Chem. Ref. Data* **1988**, 17, 513–886. https://doi.org/10.1063/1.555805
25. Umair, M.; Kanwal, T.; Loddo, V. *Catalysts* **2023**, 13, 1440. https://doi.org/10.3390/catal13111440
26. Bai, X.; Chen, W.; Wang, B. *Int. J. Mol. Sci.* **2022,** 23, 8130. https://doi.org/10.3390/ijms23158130
27. Khan, S.; Noor, T.; Iqbal, N. *ACS Omega* **2024,** 9, 14087–14099. https://doi.org/10.1021/acsomega.4c0088.
28. Ajmal, A.; Majeed, I.; Malik, R. N. *RSC Adv*. **2014**, 4, 37003–37026. https://doi.org/10.1039/C4RA06658H
29. Nemiwal, M.; Zhang, T. C.; Kumar, D. *Sci. Total Environ*. **2021,** 767, 144896. https://doi.org/10.1016/j.scitotenv.2020.144896

30. Nematov, D. *Preprints* **2024,** 202408, 1733. https://doi.org/10.20944/preprints202408.1733.v1
31. Thomas, M.; Natarajan, T. Book Chapter; **2018**. https://doi.org/10.21741/9781945291593-2
32. Wach, A.; Zou, X.; Wojtaszek, K. X-Ray *Spectrom.* **2023,** 52, 3363. https://doi.org/10.1002/xrs.3363
33. Gondal, M. A.; Dastageer, M. A.; Hameed, A. *Renewable Sustainable Energy Rev.* **2018**, 82, 181–197. https://doi.org/10.1016/j.rser.2017.07.046
34. Kumar, S.; Sharma, A.; Arya, S. *Catalysts*, 2024, 14, 420. https://doi.org/10.3390/catal14070420
35. Armaković, S. J.; Armaković, S.; Bilić, A. *Catalysts* **2025,** 15, 793. https://doi.org/10.3390/catal15080793
36. AlMohamadi, H.; Awad, S. A.; Sharma, A. K. *Catalysts* **2024,** 14, 420. https://doi.org/10.3390/catal14070420
37. Demir, A.; Aslan, F.; Esen, H. J. Mater. Sci.: *Mater. Electron*. **2024,** 35, 13213. https://doi.org/10.1007/s10854-024-13213-z
38. Zeinali Heris, S.; Bagheri Khaniani, P.; Mousavi, S. B. *J. Water Process Eng*. **2025,** 58, 107040. https://doi.org/10.1016/j.jwpe.2025.107040
39. Ge, M.; Guo, C.; Zhu, X. *Front. Environ. Sci. Eng. China* **2009,** 3, 122–127. https://doi.org/10.1007/s11783-009-0035-2
40. Hu, L.; Xing, M.; He, X. *J. Mater. Sci.: Mater. Electron.* **2023,** 34, 11690. https://doi.org/10.1007/s10854-023-11690-2
41. Mirda, E.; Idroes, R.; Khairan, K. *Polymers* **2021,** 13, 3990. https://doi.org/10.3390/polym13223990
42. Kansal, S. K.; Kundu, P.; Sood, S. New *J. Chem.* **2014,** 38, 2310–2318. https://doi.org/10.1039/C3NJ01619F
43. Boxiang, B. Z.; Hongdong, H. S.; Honglei, H. Z. Beilstein *J. Nanotechnol***. 2022**, 13, 566–575. https://doi.org/10.3762/bjnano.13.52
44. Masahiro, M.; Akira, N.; Toshiya, W. *Chem. Mater*. **2002,** 14, 410–418. https://doi.org/10.1021/cm020076p
45. Cullity, B. D. Elements of X-Ray Diffraction; *Addison-Wesley*: Reading, MA, **1978**.
46. Li, J.; Yan, L.; Wang, Y. J. *Mater. Sci.: Mater. Electron*. **2016**, 27, 10732–10739. https://doi.org/10.1007/s10854-016-4773-1
47. Shan, G.; Zhong, M.; Wang, S. *J. Colloid Interface Sci.* **2008**, 325, 456–462.

https://doi.org/10.1016/j.jcis.2008.06.027
48. Potle, V. D.; Shirsath, S. R.; Bhanvase, B. A. *Optik* **2020**, 219, 164555. https://doi.org/10.1016/j.ijleo.2020.164555
49. Babu, K. S.; Narayanan, V. *Chem. Sci. Trans.* **2013**, 2, 146–152
50. Grujić-Brojčin, M.; Šćepanović, M.; Dohčević-Mitrović, Z. *Sci. Sinter*. **2006**, 38, 183–189. https://doi.org/10.2298/SOS0602183G
51. Jing, L.; Xin, B.; Yuan, F. *J. Phys. Chem. B* **2006**, 110, 17860–17865. https://doi.org/10.1021/jp063148z
52. Wei, X.; Li, R.; Xu, Q. Sci. Rep. 2018, 8, 1–10.
53. Papitha, R.; Hadkar, V.; Sishu, N. K. *Ceram. Int*. **2024**, 50, 1–12. https://doi.org/10.1016/j.ceramint.2024.07.277
54. Resmi, V. R.; Soney, J. M.; Dhannia, T. *Opt. Mater*. **2025**, 168, 117440. https://doi.org/10.1016/j.optmat.2025.117440
55. Pan, Z.; Zhang, Q.; Song, M. *Acta Photonica Sin.* **2022**, 51, 0416001. https://doi.org/10.3788/gzxb20225104.0416001
56. Boudechiche, N.; Morante, N.; Sannino, D. *Catalysts* **2024**, 14, 883. https://doi.org/10.3390/catal14120883
57. Cozzolino, V.; Coppola, G.; Calabrò, V. *Appl. Water Sci*. **2025**, 15, 243. https://doi.org/10.1007/s13201-025-02493-3
58. Karimi, P.; Baneshi, M. M.; Malakootian, M. Desalin. *Water Treat*. **2019**, 149, 1–10. https://doi.org/10.5004/dwt.2019.24317
59. Ahmed, M. A.; El-Katori, E. E.; Gharni, Z. H. *J. Alloys Compd*. **2013**, 553, 19–29. https://doi.org/10.1016/j.jallcom.2012.10.038
60. Lin, H.; Wang, X.; Yu, P. *RSC Adv*. **2014**, 4, 37003–37026. https://doi.org/10.1039/C4RA06658H
61. Herrmann, J. M. *Catal. Today* **1999**, 53, 115–129. https://doi.org/10.1016/S0920-5861(99)00107-8
62. Gogate, P. R.; Pandit, A. B. *Adv. Environ. Res*. **2004**, 8, 501–551. https://doi.org/10.1016/S1093-0191(03)00032-7
63. Patrocinio, A. O. T.; Schneider, J.; França, M. D. *RSC Adv*. **2015**, 5, 70536–70545. https://doi.org/10.1039/C5RA13291F
64. Cheng, C.; Amini, A.; Zhu, C.; et al. *Sci. Rep.* **2014**, 4, 4181. https://doi.org/10.1038/srep04181
65. Umbrajkar, V.; Kaladagi, M. *Mater. Sci. Eng., B* **2025**, 304, 118239.

https://doi.org/10.1016/j.mseb.2025.118239

66. Ballari, M. M.; Edelmannová, M. F.; Ricka, R.; Reli, M.; Kočí, K. *Energy Convers. Manage. X* **2024**, 23, 100651. https://doi.org/10.1016/j.ecmx.2024.100651
67. Anil, K.; Surenjan, A. *Water Pract. Technol*. **2024**, 19, 1–12. https://doi.org/10.2166/wpt.2024.022
68. Landge, V. K.; Huang, C. M.; Hakke, V. S. *Catalysts* **2022**, 12, 605. https://doi.org/10.3390/catal12060605
69. Ranjith, K. S.; Rajendra Kumar, R. T. *RSC Adv*. **2017**, 7, 2036–2046. https://doi.org/10.1039/C6RA27380G
70. Alam, U.; Khan, A.; Ali, D. RSC Adv. **2018**, 8, 20345–20357. https://doi.org/10.1039/C8RA01638K
71. Navidpour, A. H.; Ahmed, M. B.; Zhou, J. L. *Nanomaterials* **2024**, 14, 135. https://doi.org/10.3390/nano14020135
72. Kumar, P.; Singh, V.; Kundu, V. *Bio Nanoscience* **2017**, 7, 505–515. https://doi.org/10.1007/s12951-017-0453-6
73. Wang, Y.; Zhang, X.; Liu, *J. Appl. Surf. Sci*. **2017**, 391, 630–639. https://doi.org/10.1016/j.apsusc.2016.07.064
74. Duca, M.; Li Puma, G.; Smirniotis, P. G. *Chem. Eng. J.* **2010**, 161, 1–9. https://doi.org/10.1016/j.cej.2009.10.045
75. Li, D.; Zhang, X.; Yu, *J. Appl. Catal., B* **2019**, 243, 537–548. https://doi.org/10.1016/j.apcatb.2018.11.001
76. Lim, N. Y. Y.; Chiam, S. L.; Leo, C. P. *Hybrid Adv*. **2024**, 7, 100318. https://doi.org/10.1016/j.hybadv.2024.100318
77. Ghamarpoor, R.; Fallah, A.; Jamshidi, M. *ACS Omega* 2024, 9, 11230–11245. https://doi.org/10.1021/acsomega.3c08717
78. Baradaran, M.; Ghodsi, F.; Bittencourt, C. *J. Alloys Compd*. **2019**, 788, 1133–1142. https://doi.org/10.1016/j.jallcom.2019.02.184
79. Chakravorty, A.; Roy, S. *Sustainable Chem. Environ*. **2024**, 2, 100155. https://doi.org/10.1016/j.scenv.2024.100155
80. Zhang, L. Y.; Yang, J. J.; You, Y. H. *RSC Adv.* **2021**, 11, 38265–38275. https://doi.org/10.1039/D1RA07757K